



## BIROn - Birkbeck Institutional Research Online

Wei, F. and Prytulak, J. and Xu, J. and Wei, W. and Hammond, James O.S. and Zhao, B. (2017) The cause and source of melting for the most recent volcanism in Tibet: a combined geochemical and geophysical perspective. *Lithos* 288-9 , pp. 175-190. ISSN 0024-4937.

Downloaded from: <https://eprints.bbk.ac.uk/id/eprint/19274/>

*Usage Guidelines:*

Please refer to usage guidelines at <https://eprints.bbk.ac.uk/policies.html> or alternatively contact [lib-eprints@bbk.ac.uk](mailto:lib-eprints@bbk.ac.uk).

1 The cause and source of melting for the most recent  
2 volcanism in Tibet: a combined geochemical and  
3 geophysical perspective  
4

5 Feixiang Wei<sup>1,2</sup> weifeixiang@ies.ac.cn

6 Julie Prytulak<sup>2</sup> j.prytulak@imperial.ac.uk

7 Jiandong Xu<sup>1</sup> xujiandong@ies.ac.cn

8 Wei Wei<sup>1</sup> weiwei25011@gmail.com

9 James O. S. Hammond<sup>3</sup> j.hammond@ucl.ac.uk

10 Bo Zhao<sup>1</sup> zhaobo@ies.ac.cn

11  
12 1 Key Laboratory of Active Tectonics and Volcano, Institute of Geology, China  
13 Earthquake Administration, Beijing 100029, China.

14 2 Department of Earth Science and Engineering, Imperial College London SW7 2AZ,  
15 UK.

16 3 Department of Earth and Planetary Sciences, Birkbeck College, University of  
17 London, London WC1E 7HX, UK.

18  
19 Abstract

20 We investigate the youngest volcanic activity on the Tibetan Plateau by combining  
21 observations from petrologic, geochemical and seismic tomography studies. Recent  
22 (from 2.80 Ma to present) post-collisional potassium-rich lavas from the Ashikule

23 Volcanic Basin (AVB) in northwestern Tibet are characterised by remarkably enriched  
24 light rare earth elements (LREE) relative to heavy rare earth elements (HREE), and  
25 enriched large ion lithophile element (LILE) relative to high field strength elements  
26 (HFSE). Strontium and neodymium isotopic compositions are surprisingly restricted,  
27 and show little evidence for mixing or crustal contamination, despite the thick crust  
28 upon which they are erupted. Geochemical characteristics indicate a homogeneous  
29 source, highly enriched in trace elements, which is most consistent with derivation  
30 from long-lived subcontinental lithospheric mantle (SCLM). P-wave anisotropy  
31 tomography documents a gap between the north-subducting Indian slab and  
32 south-subducting Tarim slab directly beneath the AVB. We propose that volcanism in  
33 northwestern Tibet is associated with the progressive closure of this gap, during which  
34 shear heating of the SCLM can generate localised melting, with deep-seated faults  
35 providing a mechanism for erupted lavas to escape large-scale crustal contamination  
36 and fractionation in magma reservoirs. Thus, shear heating may provide an  
37 explanation for the restricted range of radiogenic isotope compositions from a SCLM  
38 source that should be, by its nature, heterogeneous on a large scale.

39

40 *Key words*

41 *Tibetan Magmatism, Shoshonite. Lithospheric Mantle, Tarim Block, Shear Heating*

42

## 43 1. Introduction

44 The Tibetan Plateau is the most protuberant structure on Earth, formed in

45 response to the collision of the Indian and Asian plates from 50-55 Ma ago (e.g.,  
46 Royden et al., 2008; Tapponnier et al., 2001). Since the initial collision, the Indian  
47 Plate has continued to subduct northward with recent studies depicting it  
48 underthrusting the entire Tibetan Plateau to its northwestern margin and colliding with  
49 the south-directed subducting Tarim Block (e.g., Tunini et al., 2016, Wei et al., 2015,  
50 2016; Zhao et al., 2010). Collision with the Tarim block likely contributed to the rapid  
51 uplift of the Tibetan Plateau at ~13 Ma (Turner et al., 1993), and resulting global  
52 climate change (e.g., Kutzbach et al., 1993; Zhisheng et al., 2001).

53 A striking feature of the plateau, and northern Tibet in particular, is its widespread  
54 Cenozoic post-collisional magmatism, which is distributed between 78°E and 92°E  
55 and between 34°N and 36°N, forming a volcanic belt ~1300 km in length with a 100  
56 km western and 400 km eastern width (e.g., Arnaud et al., 1992; Chung et al., 2005;  
57 Cooper et al., 2002; Ding et al., 2003; Guo et al., 2006, 2014; Royden et al., 2008;  
58 Turner et al., 1993, 1996; Wang et al., 2005; Xia et al., 2011). This volcanic belt  
59 consists of more than fifty volcanic clusters that can be spatially divided into four  
60 domains: (1) the Qiangtang volcanic area; (2) the Hoh Xil and middle Kunlun  
61 volcanic area; (3) the west Kunlun volcanic area; (4) the Karakoram volcanic area  
62 (Mo et al., 2006). The rich literature of previous studies on the post-collision lavas in  
63 north Tibet shows that these Cenozoic K-rich lavas generally show remarkable  
64 enrichment of LILE and LREE relative to HFSE and HREE. The petrogenesis of  
65 K-rich continental lavas in Tibet, and in general worldwide, is a topic of long-standing  
66 debate, with hypotheses ranging from the involvement of plumes (Guo et al., 2006),

67 crustal melting (Hacker et al., 2014; Wang et al., 2005, 2016), sub-continental  
68 lithospheric mantle (Conticelli et al., 2009; Guo et al., 2015; Huang et al., 2015;  
69 Turner et al., 1993, 1996; Williams et al., 2004), and contributions from subducted  
70 slabs and recycled mélanges (Guo et al., 2014).

71 Temporally, magmatism in Tibet spans a period of ~45 Ma: 45-26 Ma in central  
72 Tibet, 26-8 Ma in southern Tibet and 20 Ma to historic activity in northern Tibet (e.g.,  
73 Guo et al., 2006, 2014; Turner et al., 1993, 1996; Williams et al., 2004; Xia et al.,  
74 2011). The most recent eruption on Tibetan Plateau occurred in 1951 AD from the  
75 Ashi Volcano in the Ashikule Volcanic Basin (AVB; Liu and Maimaiti, 1989; Xu et al.,  
76 2012, 2014).

77 Several geophysical studies suggested that the Indian plate and Tarim Block  
78 collide below the northwestern Tibetan Plateau (e.g., Tunini et al., 2016; Zhao et al.,  
79 2010). However, recent tomographic studies focussed on the AVB show that the  
80 volcanic basin is in fact located above a gap in the mantle lithosphere between the  
81 Indian plate and Tarim Block (Wei et al., 2015, 2016; Fig. 2). The upwelling of  
82 asthenospheric mantle through this gap may be responsible for the generation of the  
83 Ashikule volcanoes (Fig.2; Wei et al., 2015, 2016). Because of the inaccessibility of  
84 the AVB (it has an average altitude of ~4800 m and poor transport infrastructure due  
85 to the sparse human population), the petrogenesis of its lavas has not been studied  
86 systematically. The combined studies of Williams et al. (2004) and Guo et al. (2006,  
87 2014) present some chemical analyses of nine samples from the region, but focused  
88 more broadly on magmatism in the whole of northern Tibet, and thus necessarily

89 treated the limited samples from the AVB as an integrated unit. Cooper et al (2002)  
90 studied the isotopic and chemical characteristics of lavas in the youngest episode,  
91 which are only a part of the AVB.

92 The occurrence of present day magmatic activity and improved seismic imaging  
93 allows us to combine geochemical and geophysical information. Understanding this  
94 region has direct impact on evaluating hypotheses for the generation of continental  
95 K-rich lavas in general and on the style and evolution of magmatism across northern  
96 Tibet in particular. We present whole rock major, trace and Sr-Nd isotopic  
97 compositions of 25 lavas encompassing all six volcanic episodes in the AVB  
98 suggested by Liu and Maimaiti (1989) and Xu et al. (2014). In combination with  
99 previous chronological data (Liu and Maimaiti, 1989; Xu et al., 2014) and  
100 geophysical results (e.g., Tunini et al., 2016; Wei et al., 2015, 2016; Wittlinger et al.,  
101 2004; Zhao et al., 2010), we examine the petrogenesis of recent AVB volcanism with  
102 relation to its geodynamic setting.

103

## 104 2. Geological background

105 The AVB is located in the western Kunlun orogenic belt (Fig. 1), which marks the  
106 northwestern margin of Tibetan Plateau (Wang et al., 2003; Wang, 2004) where the  
107 Tarim Block has subducted southward, perhaps to a depth of 300 km (e.g., Tunini et  
108 al., 2016; Wei et al., 2016; Wittlinger et al., 2004; Zhao et al., 2010). Structurally  
109 controlled by Altyn Tagh, Karakax and Longmu-Gozha Co fault systems (Fig. 1a), the  
110 AVB can be characterised as a pull-apart basin (Li et al., 2006), suffering dominantly

111 EW extensional stress and shearing (Furuya and Yasuda, 2011; Xu et al., 2012). The  
112 AVB is seismically active and three strong earthquakes have occurred close to this  
113 basin in 2008 (Mw 7.1), 2012 (Mw 6.2) and 2014 (Mw 6.9) (Fig. 1a; Bie and Ryder,  
114 2014). The 2008 Yutian earthquake (Mw 7.1) ruptured a normal fault in the AVB,  
115 resulting in a surface rupture zone of up to 50 km (Bie and Ryder, 2014; Elliott et al.,  
116 2010; Furuya and Yasuda, 2011; Xu et al., 2013).

117 The AVB covers an area of  $\sim 700 \text{ km}^2$  and encompasses 14 main volcanoes, with  
118 activity spanning from 2.80 Ma to 1951 AD (Fig. 1b). The main volcanological  
119 features in the region are volcanic cones, lava terraces and lava valleys (Xu et al.,  
120 2012). The largest and highest volcano in the basin is Dahei volcano, which has an  
121 altitude of  $\sim 5090$  m above sea level and a relative altitude of  $\sim 350$  m. Most volcanoes  
122 in the basin are characterised by explosive eruptions (e.g., Ashi, Dahei and Wuluke  
123 volcanoes), accompanied by some effusive eruptions in the west and east of the basin  
124 (e.g., Xishan volcano and Dongshan volcanoes). Chronological studies (Liu and  
125 Maimaiti, 1989; Xu et al., 2014) show that most volcanoes were active in the  
126 Quaternary. Six episodes of volcanic activity have been defined as follows: 1. Late  
127 Ashi Episode (in 1951; Liu and Maimaiti, 1989), 2. Ashi Episode (0.12-0.17 Ma), 3.  
128 Wuluke Episode (0.20-0.29 Ma), 4. Dahei Episode (0.46-0.60 Ma), 5. Mati Episode  
129 (1.02-1.65 Ma), 6. Xi Episode (2.34-2.8 Ma).

130

### 131 3. Sample selection and petrography

132 Two field campaigns were conducted by Institute of Geology, China Earthquake

133 Administration in May of 2011 and 2015 where over 140 lava samples were collected.  
134 From these, twenty-five representative samples were chosen to cover the main  
135 volcanoes in the AVB according to the geological map (Fig. 1b) revised from Xu et al.  
136 (2014) and Liu and Maimaiti (1989). A thin section of each sample was made for  
137 petrographic analysis from the same material as was processed for whole-rock  
138 chemistry.

139 All lavas studied are porphyritic, with phenocrysts of plagioclase, clinopyroxene,  
140 orthopyroxene, phlogopite, rare olivine and Fe-Ti oxides in a ground-mass consisting  
141 of volcanic glass, plagioclase laths, clinopyroxene, orthopyroxene and rare olivine  
142 and Fe-Ti oxides (visually estimated volume percentages are presented in Table 1).  
143 The dominant phenocryst phase is plagioclase, which displays a notable lack of  
144 commonly developed zoning. All samples are vesicular, ranging from 10% to 80% by  
145 volume. A low degree of vesicular refilling by secondary minerals (calcite and clay  
146 minerals) is petrographically present in some samples (ASKL-15, ASKL-16,  
147 ASKL-17, ASKL-18, 515-1, 516-2). These obvious alteration products were removed  
148 by hand-picking the crushate before reducing the sample to powder. The phenocrysts  
149 and groundmass of analysed samples are unaltered. Figure 3 depicts representative  
150 textures encountered in the AVB lavas.

151

## 152 4. Methods

### 153 4.1. Major and trace element analysis

154 Visibly altered portions of the rocks were removed and fresh material was

155 reduced to centimetre size by jaw crusher. Material was then hand-picked and  
156 hand-crushed in agate mortar to fine powders for whole-rock major, trace element and  
157 Sr-Nd analysis. Whole-rock major element analysis was conducted by X-ray  
158 fluorescence (XRF) at Activation Laboratories Ltd. (Ontario, Canada;  
159 [www.actlabs.com](http://www.actlabs.com)).

160 High-precision trace element analysis was undertaken at the Open University, UK,  
161 with an Agilent 8800 ICP-QQQ ('triple-quad' inductively coupled plasma mass  
162 spectrometer). Sample digestion was performed at the Mass Spectrometry and  
163 Geochemistry Labs at Imperial College London (MAGIC). Approximately 100 mg of  
164 rock powder was dissolved in sealed Teflon vials with a 3:1 mixture of distilled  
165 concentrated HF: HNO<sub>3</sub>. The solutions were ultra-sonicated for 25 minutes and heated  
166 at 160 °C hot plate for at least 24 hours. They were then evaporated to near dryness  
167 and re-dissolved in 2 ml distilled 6M HCl at 120 °C for at least 24 hours. The  
168 solutions were then evaporated to complete dryness at 120 °C and re-dissolved in ~1  
169 ml concentrated HNO<sub>3</sub> and evaporated at 180 °C. The last re-dissolution and  
170 evaporation step was repeated at least three times until the samples turned brownish  
171 or brown, indicating the destruction of fluorides from initial HF dissolution. Finally, 2%  
172 distilled HNO<sub>3</sub> was added to samples for a 1000-fold dilution.

173 Diluted samples were aspirated into the ICP-MS using a quartz microflow  
174 nebuliser, with an uptake rate of 0.5ml per minute, and count rates in the order of 1 –  
175  $5 \times 10^7$  cps/ppm. Analyses were performed in three different collision/reaction cell  
176 modes (no gas, He, O<sub>2</sub> mass shift). Oxide levels (measured as CeO/Ce) were kept low,

177 at 1% in no gas, and 0.5% in He collision mode, and doubly charged species  
178 ( $\text{Ce}^{++}/\text{Ce}^{+}$ ) at 1.6% in no gas, and 1.2% in He collision mode. Analyses were  
179 standardised against five reference materials (digested at both the Open University  
180 and Imperial College London) that were measured at the beginning of each analytical  
181 run. The reference materials were selected on the basis of their similarity to the  
182 samples analysed, and include BIR-1, W-2, GSP-2, BHVO-2 and AGV-1. An internal  
183 standard solution (consisting of Be, Rh, In, Tm, Re, and Bi) was added to samples and  
184 run on-line throughout all analyses to correct for any instrumental drift. Drift was  
185 further monitored with a measurement block consisting of USGS reference material  
186 BIR-1 (separate digest to that used in the standardisation), a 2%  $\text{HNO}_3$  blank, and a  
187 repeated unknown sample (ASKL-7) performed every five unknown measurements.

188

## 189 *4.2. Sr-Nd isotopes*

### 190 *4.2.1. Chemical isolation of Sr and Nd*

191 Approximately 50 mg of sample powder was leached following the method of  
192 Weis and Frey (1991, 1996) and digested using the same method as trace element  
193 digestion described above. Strontium and Nd were separated by a three-stage column  
194 chemistry. The first column employs 1.4 ml volume Bio-Rad AG50X8 200-400 mesh  
195 cation exchange resin, to separate Sr and rare earth elements (REE) from the sample  
196 matrix. Samples were loaded with 1M HCl, and the Sr fractions were collected in 4  
197 ml 3M HCl and 0.5 ml 6M HCl. REE cuts were subsequently collected in 6.5 ml 6M  
198 HCl. The second column purifies the Sr fraction using 100  $\mu\text{l}$  shrink Teflon columns

199 and 100-150 mesh Eichrom Sr resin. Strontium fractions were loaded with 300 ul 3M  
200 HNO<sub>3</sub> and purified Sr solutions were collected with 4 ml 0.05M HNO<sub>3</sub>. The third  
201 stage column chemistry separates Nd from the REEs using a Teflon column loaded  
202 with 1 mL of Eichrom Ln-Spec resin (100-150 um). REE cuts were loaded with 200  
203 ul 0.2M HCl and Nd was collected in 6 ml 0.2M HCl.

204

#### 205 *4.2.2. Mass Spectrometry*

206 Strontium and neodymium isotopic analyses were performed in the MAGIC  
207 laboratories at Imperial College London. Strontium isotopes employed a Thermo  
208 Finnigan Triton thermal ionization mass spectrometer (TIMS) whilst Nd isotope  
209 analysis used a Nu Instruments HR Multi-collector Inductively Coupled Plasma Mass  
210 Spectrometer (MC-ICPMS).

211 Strontium fractions were dissolved in 6M distilled HCl and loaded on single  
212 zone-refined rhenium filaments, with a TaCl<sub>5</sub> activator to enhance Sr ionization.  
213 Faraday cups collected masses <sup>83</sup>Kr, <sup>84</sup>Sr, <sup>85</sup>Rb, <sup>86</sup>Sr, and <sup>88</sup>Sr on channels L4, L3, L2,  
214 L1, C, and H1, respectively. Data were collected in static mode with virtual amplifier  
215 rotation, using a dummy mass of <sup>83</sup>Kr in L4. Measurement consisted of 12 blocks of  
216 15 cycles with an electronic baseline between each block. Mass fractionation was  
217 corrected online using <sup>86</sup>Sr/<sup>88</sup>Sr = 0.1194 and the exponential law. Potential  
218 contribution of <sup>87</sup>Rb on <sup>87</sup>Sr was corrected online using <sup>87</sup>Rb/<sup>85</sup>Rb = 0.3856. Standard  
219 NIST SRM 987 was measured before and during measurement sessions and unknown  
220 samples were normalised to the accepted value of <sup>87</sup>Sr/<sup>86</sup>Sr = 0.710248 (Thirlwall,

221 1991).

222 Neodymium fractions were re-dissolved in 0.1M HNO<sub>3</sub> for analysis by  
223 MC-ICPMS. Samples were introduced as 50 ppb solutions via a Nu DSN-100  
224 Desolvation Nebuliser System. Masses <sup>138</sup>Ba, <sup>140</sup>Ce, <sup>142</sup>Nd, <sup>143</sup>Nd, <sup>144</sup>Nd, <sup>145</sup>Nd, <sup>146</sup>Nd,  
225 <sup>147</sup>Sm, <sup>148</sup>Nd were collected on Faraday cups L4, L3, L2, L1, C, H1, H2, H3, and H4,  
226 respectively. Measurements were collected in three blocks of 20 cycles, with an  
227 electronic baseline in between blocks. Mass fractionation was corrected using  
228 <sup>146</sup>Nd/<sup>145</sup>Nd = 0.7219 and the exponential law. Neodymium standard JNdi was  
229 measured at the beginning and during the measurement session, and unknown  
230 samples were normalised according to the offset of JNdi in a single measurement  
231 session from its accepted value (<sup>143</sup>Nd/<sup>144</sup>Nd = 0.512115; Tanaka et al., 2000).

232

## 233 5. Results

### 234 5.1. Whole rock major and trace elements

#### 235 5.1.1. Major elements

236 United States Geological Survey (USGS) basaltic reference materials BIR-1a and  
237 BHVO-2 were processed as unknowns for whole rock major element analyses and are  
238 in good agreement with accepted values (see supplemental information). Whole rock  
239 major element concentrations for AVB lavas are presented in Table 2. The samples  
240 yield SiO<sub>2</sub> contents between 45.91 and 59.48 wt%. For classification, the major  
241 element compositions were recalculated to 100% on an anhydrous basis, and plotted  
242 on the total alkali versus silica (TAS) diagram (Fig. 4a). Most samples plot within the

243 trachyandesite field, with several relatively old samples (ASKL-14, ASKL-17,  
244 ASKL-18, 516-11, 516-12) within the basaltic trachyandesite, phonotephrite and  
245 basanite fields. Samples greater than 2 Ma, in particular, lie at distinctly higher total  
246 alkali contents for their degree of evolution than the rest of the samples. In general, all  
247 samples are characterised by high K<sub>2</sub>O (3.48-4.47 wt%) and K<sub>2</sub>O/Na<sub>2</sub>O ratios (1.08 –  
248 1.53) (Fig. 4b), and belong to the shoshonitic series. MgO contents range from 2.24 to  
249 7.40 wt% with Mg# of 46 to 63, displaying negative correlations with SiO<sub>2</sub> contents  
250 (Fig. 5a and Fig. 5b). One young sample (ASKL-3) from the recent eruption at Ashi  
251 Volcano, and 4 relatively old samples (ASKL-17, ASKL-18, 516-11, 516-12) exhibit  
252 higher MgO contents and Mg# numbers compared with other AVB samples. Given  
253 that the lavas are not co-genetic, distinct liquid lines of descent cannot be constructed.  
254 However, Fe<sub>2</sub>O<sub>3(T)</sub> (5.96-10.04 wt%) and CaO (5.15-9.39 wt%) contents display  
255 negative correlations with SiO<sub>2</sub>, consistent in general with the fractionation of mafic  
256 phases. TiO<sub>2</sub> (1.36-2.22 wt%) and Al<sub>2</sub>O<sub>3</sub> (12.69-14.97 wt%) have less distinct  
257 correlations with SiO<sub>2</sub>, but support the extensive plagioclase fractionation and the  
258 presence of oxides observed in thin sections (Fig. 5; Table 1).

259

### 260 *5.1.2. Trace elements*

261 Trace element compositions are given in Table 2. Based on repeated analyses of  
262 sample ASKL-7 and USGS standard BIR-1a, the reproducibility of most elements was  
263 better than 2% and the measured values of standards deviate < 5% from  
264 recommended values for most elements (see supplementary information). Total

265 procedural blanks from digestion at MAGIC are also given in the supplemental  
266 information and are negligible compared to the concentration of elements measured.

267 A primitive mantle normalised incompatible element plot is presented in Fig. 6a,  
268 whilst a chondrite-normalised REE pattern is depicted in Figure 6b. Figure 6  
269 illustrates the markedly elevated trace element concentrations of AVB lavas,  
270 consistent with K-rich continental magmatism in general. The AVB samples are all  
271 very similar in trace element composition, despite covering a range of > 2 Ma. They  
272 are characterised by significant positive Ba, Th, Pb and Nd anomalies and negative  
273 Nb, Ta, Zr and Ti anomalies. For comparison, the most isotopically enriched mantle  
274 endmember composition of “EM II” calculated for Samoan ocean island basalts  
275 (Jackson et al., 2007), global subducting sediment (GLOSS; Plank and Langmuir,  
276 1998) and average upper continental crust (UCC, Rudnick and Gao, 2003) are also  
277 plotted. It is noteworthy that the enrichment of LILEs and LREEs in AVB lavas is  
278 more pronounced than all of the comparative suites.

279 The AVB lavas have  $(La/Yb)_n$  ratios of 40 to 68, which correlate negatively with  
280 MgO contents (Fig. 7a) and positively with  $La_n$  (La composition normalised to  
281 primitive mantle, 131 to 295; Fig. 7b). All samples in the AVB are characterised by  
282 negative Eu anomalies ( $Eu/Eu^* < 1$ ), which correlate positively with MgO contents,  
283 consistent with plagioclase fractionation (Fig. 7c). Titanium anomalies ( $Ti/Ti^*$ ) show  
284 negative correlation with  $SiO_2$ , consistent with oxide fractionation (Fig. 7d). Ba/Th  
285 ratios correlate negatively with Th/Nd ratios, whilst Th/La ratios show less distinct  
286 negative correlation with Sm/La ratios (Fig. 7e and Fig. 7f).

287

288 *5.2. Sr-Nd isotope geochemistry*

289 Table 3 presents Sr and Nd isotopic data for the AVB samples. USGS reference  
290 materials BCR-2, BHVO-2 and BIR-1a were processed with all unknown samples and  
291 are in excellent agreement with literature values (see supplemental information).  
292 Despite the fresh appearance of samples in the field and the effort to exclude potential  
293 alteration phase during creation of rock powders, we performed leaching tests on the  
294 rock powders to exclude the effect of potential secondary alteration phases. Initial  
295 tests of leached versus unleached powders showed no discernible difference in Nd  
296 isotopes, but significant differences in Sr isotopes of up to 1640 ppm (see  
297 supplemental information), thus all rock powders were leached according to the  
298 method of Weis and Frey (1991, 1996).

299 All lavas have enriched  $^{87}\text{Sr}/^{86}\text{Sr}$  (0.707490 – 0.710523) and  $^{143}\text{Nd}/^{144}\text{Nd}$   
300 (0.512265 – 0.512472) relative to bulk silicate earth (BSE) (Fig. 8).  $^{87}\text{Sr}/^{86}\text{Sr}$  and  
301  $^{143}\text{Nd}/^{144}\text{Nd}$  plot away from the bulk silicate Earth towards the enriched mantle II  
302 endmember of Zindler and Hart (1986). The AVB data is remarkably restricted, with  
303 two outliers belonging to the > 2 Ma lavas, which display slightly less radiogenic Sr  
304 and more radiogenic Nd. Our data are in good accordance with the isotopic results of  
305 younger lavas measured by TIMS (Cooper et al., 2002). Additionally, our most  
306 primitive sample (ASKL-18) has similar Sr-Nd isotopic ratios to comparable literature  
307 samples AH602 and AH609 of Guo et al. (2014).

308

## 309 6. Discussion

310 We examine the petrogenesis of the AVB lavas and attempt to link chemical and  
311 isotopic information with the unique tectonic setting as depicted by recent seismic  
312 tomography (Wei et al., 2016). First, we assess modifications to the primary lava  
313 signature. We then examine and evaluate common models for the generations of  
314 continental K-rich magmas to determine the most likely petrogenesis of the AVB  
315 lavas. Finally, we integrate recent seismic observations with geochemistry for a richer  
316 understanding of the interplay of tectonics and magma generation in the region.

317

### 318 *6.1. Fractional crystallisation and crustal contamination*

319 Due to the collision between the Indian and Asian plates, the thickness of the  
320 crust in northwestern Tibet has reached up to 90 km (Tunini et al., 2016; Wittlinger et  
321 al., 2004). Thus, there is ample opportunity for fractional crystallisation in crustal  
322 magma chambers and crustal assimilation to modify the chemical signature of  
323 magmas after they leave their source region(s).

324 Petrographic investigations of the Ashi Volcano carried out by Yu et al. (2014)  
325 proposed mixing between two crustal magma pockets based on distinct zoned  
326 phenocryst populations of pyroxene and plagioclase cores and rims.  
327 Orthopyroxene-liquid thermometry was used to estimate magmatic equilibrium  
328 temperature and pressure conditions, suggesting that an evolved magma pocket  
329 (13-18 km in depth) may connect with a deeper trachyandesite magma pocket (18-30  
330 km in depth). Yu et al. (2014) speculated that because the two magma pockets are

331 vertically connected, the evolved magma pocket may be generated by fractional  
332 crystallisation of the trachyandesite magma. Beyond the petrographic analysis of Yu  
333 et al. (2014), there are only sparse reports of evolved erupted lavas in the region by  
334 Deng et al. (1998).

335 The impact of fractional crystallisation can be generally demonstrated in our  
336 dataset. For example, the correlations between Eu anomaly and MgO, and between Ti  
337 anomaly and SiO<sub>2</sub> (Fig. 7c, 7d), provide evidence for plagioclase and oxide  
338 fractionation, respectively. These phenocryst phases are also observed  
339 petrographically (Table 1). Among the younger samples, the youngest episode lavas  
340 (ASKL-3, ASKL-4 and 518-5) have the highest MgO contents, suggesting lowest  
341 degrees of fractional crystallisation. Therefore, the most recent eruption may be  
342 related to new magma inputs from the source.

343 With the exception of the three oldest samples (ASKL-17, ASKL-18, 516-11),  
344 Sr-Nd isotopic ratios are remarkably uniform (Fig. 8). The restricted Sr-Nd signature  
345 of the younger samples suggests a homogenous source, which is also supported by  
346 their similar trace element patterns (Fig. 6). In plots of SiO<sub>2</sub> versus <sup>87</sup>Sr/<sup>86</sup>Sr and  
347 <sup>143</sup>Nd/<sup>144</sup>Nd (Fig. 9a and Fig. 9b), younger samples do not show significant variation  
348 of Sr and Nd isotopes over a modest range of SiO<sub>2</sub> contents (53.78% to 59.48%).  
349 Therefore, despite the thick continental crust, significant crustal contamination in the  
350 younger AVB lavas are unlikely, as no correlation with SiO<sub>2</sub> contents are observed. It  
351 is also difficult to reconcile how crustal assimilation would produce near-identical  
352 Sr-Nd isotope compositions over million year timescales. Additionally, the LILEs and

353 LREEs of the AVB lavas (i.e., Rb, Sr, Sm and Nd concentrations) are significantly  
354 higher than those typically found in the continental crust (Fig. 6). Therefore, the  
355 effects of crustal assimilation are not necessarily apparent in these lavas from simple  
356 mass balance considerations. Thus, although some degree of crustal contamination  
357 seems inevitable, it is unlikely to modify the magmatic chemistry significantly.

358

### 359 *6.2. Petrogenesis of the AVB lavas from geochemical considerations*

360 Modification by fractional crystallisation does not affect long-lived radiogenic  
361 Sr-Nd isotope compositions and should therefore provide information about magmatic  
362 source(s). Guo et al. (2014) proposed that post-collisional K-rich magmatism in  
363 northern Tibet reflects subduction-related metamorphic mélanges. They suggested  
364 mélange zones on top of both the Indian and Tarim subducting slabs mix slab  
365 materials and mantle rocks. These mixed mélanges are fluid-rich and thus buoyant,  
366 and subsequently upwell and partially melt to high degrees. This model does not  
367 include a means of focussing volcanism and explicitly involves materials with a range  
368 of isotope compositions. For example, the Indian and Tarim slabs are isotopically  
369 distinct (Tarim block,  $^{87}\text{Sr}/^{86}\text{Sr} \approx 0.708$  and  $^{143}\text{Nd}/^{144}\text{Nd} \approx 0.5119$ ; Indian plate,  
370  $^{87}\text{Sr}/^{86}\text{Sr} > 0.713$  and  $^{143}\text{Nd}/^{144}\text{Nd} < 0.5122$ ; Guo et al., 2014) and a wide range of  
371 radiogenic isotope variability is possible when considering the inaccessible  
372 sedimentary package that these slabs may host.

373 According to the spatial classification in Guo et al. (2014), the AVB belongs to  
374 the middle sub-group volcanic field, which displays variable mixing proportions of

375 the Indian and Tarim materials. The Sr-Nd isotopic signatures of the AVB lavas are  
376 extremely restricted (Fig. 8, 9), and do not conform to the notion of three  
377 endmember-mixtures (DMM, Tarim and Indian mélanges). Marschall and  
378 Schumacher (2012) proposed a ‘mélange average’ to highlight trace element  
379 similarities with arc volcanism. Even though the AVB lavas share similar  
380 characteristics of distinct enrichment in Pb and depletion in Nb, Ta and Ti, mélange  
381 abundances of LILEs and LREEs are much lower than those of the AVB lavas and the  
382 slope of the REE is markedly flatter in mélange averages compared to the AVB lavas.  
383 Although we cannot definitively rule out a small contribution from mélanges, they are  
384 highly unlikely to dominate the chemical signature of AVB lavas.

385 Tomographic images (Fig. 2) depict a low-velocity gap between the Indian and  
386 Tarim lithospheres, which may be a channel for upwelling asthenosphere (Wei et al.,  
387 2015, 2016). Derivation solely from a shallow asthenospheric, MORB-like source is  
388 inconsistent with isotopic (Fig. 8) and trace element (Fig. 6b) signatures of the AVB.  
389 The elevated trace element concentrations of AVB lavas, and K-rich continental lavas  
390 in general, require a source enriched beyond fertile primitive mantle. Given the thick,  
391 enriched continental crust in the region, it may provide such a source. Volcanism  
392 related to crustal melting has been reported in the Hohxil area of northern Tibet by  
393 Wang et al. (2005), but the K-rich “adakitic” volcanic rocks in this area exhibit high  
394 SiO<sub>2</sub> contents (61-67%). The major element features of the AVB lavas, such as their  
395 low SiO<sub>2</sub> contents (Fig. 4, 5) make it unlikely that they are derived by direct partial  
396 melting of continental crust. High source concentrations of trace elements can also be

397 achieved by multistage enrichments by small degree melt metasomatism of  
398 underlying lithosphere. Indeed, partial melting of the metasomatised sub-continental  
399 lithospheric mantle (SCLM) has often been invoked for potassic magmatism in Tibet  
400 (e.g., Cooper et al., 2002; Turner et al., 1993, 1996; Williams et al., 2004) and the  
401 western Mediterranean (e.g., Conticelli et al., 2009).

402 At face value, melting of the metasomatised SCLM appears to offer the best  
403 explanation for the chemical characteristics of the AVB lavas. The depth of melt  
404 generation can be explored using the REE and HFSE characteristics. Williams et al.  
405 (2004) compared the difference between peridotite melting models of both spinel and  
406 garnet facies. They suggested that partial melting of a spinel-facies  
407 phlogopite-bearing peridotite source was responsible for the volcanism in north Tibet.  
408 However, as the authors explained, their model cannot reproduce reasonable  
409 concentrations of yttrium, a HREE. Additionally, spinel-facies sources are  
410 inconsistent with the absence of Zr/Hf fractionation in our AVB samples (46.7-51.9;  
411 Fig. 10). Fractionation is expected, because  $D_{Zr}/D_{Hf}$  in garnet facies is around one,  
412 whilst  $D_{Zr}/D_{Hf}$  of clinopyroxene in spinel stability field is around 0.5 (Weyer et al.,  
413 2003), thus different degrees of partial melting in the spinel stability field would cause  
414 variable Zr/Hf ratios.

415 Trace element geochemistry can also provide clues about the mineralogy of the  
416 mantle source. For example, Nb-Ta, are chemical twins, having the same valency (+5)  
417 and similar ionic radii, thus, they are expected to behave congruently in both fluids  
418 and melts (e.g., Dostal and Chatterjee, 2000; Kalfoun et al., 2002; Weyer et al., 2003).

419 In Fig. 10, the AVB lavas display variable Nb/Ta ratios, significantly higher than the  
420 primitive mantle (PM), UCC, GLOSS and EM2 endmembers. Depleted Nb-Ta  
421 concentrations and high Nb/Ta ratios of the AVB lavas may be related to Ti-rich oxide  
422 minerals in the residual phases such as rutile, amphibole and phlogopite. Xenolith  
423 data from Kalfoun et al. (2002) indicate that rutile may be an important host for HFSE,  
424 which is consistent with the HFSE depletions (such as Nb, Ta, Zr and Hf) and low  
425 Ti<sub>2</sub>O content in the AVB lavas. Other alternative residual minerals are amphibole and  
426 phlogopite, which are the only Nb- and Ta-rich silicate minerals in the upper mantle  
427 (Kalfoun et al., 2002).

428 The existence of phlogopite in the upper mantle has long been demonstrated by  
429 petrological studies (e.g., Kushiro et al., 1968; Sudo and Tatsumi, 1990; Wyllie and  
430 Sekine, 1982). In Fig. 4, K<sub>2</sub>O contents are high, but similar (3.48-4.47 wt%) over a  
431 comparatively wide range of SiO<sub>2</sub> (45.91-59.48%). In combination with the relatively  
432 low MgO contents of the AVB lavas, these characteristics indicate buffering of K<sub>2</sub>O  
433 by potassium-rich phases in the mantle source (i.e., phlogopite and/or amphibole).  
434 Because Rb and Ba are compatible in phlogopite, whilst Rb, Sr and Ba are moderately  
435 compatible in amphibole, melts in equilibrium with phlogopite have high Rb/Sr and  
436 lower Ba/Rb ratios than that formed in amphibole-bearing source. As suggested by  
437 Furman and Graham (1999) and Yang et al. (2004), samples with low Ba/Rb (<20)  
438 and high Rb/Sr (>0.1) are generally derived from phlogopite-bearing source. In Fig.  
439 11, the plot of Rb/Sr versus Ba/Rb ratios implies that the AVB lavas are derived from  
440 a phlogopite-rich source.

441 The ~90 km-thick crust (Tunini et al., 2016; Wittlinger et al., 2004) suggests that  
442 the SCLM is deep with high temperature and pressure. Phlogopite is more stable than  
443 amphibole at these P-T conditions (Condamine and Medard, 2014; Sudo and Tatsumi,  
444 1990). Therefore, we suggest that the AVB lavas are likely derived by partial melting  
445 of the Tibetan phlogopite-garnet-bearing SCLM. This result is in accordance with  
446 melting experiments conducted by Condamine et al. (2016), which suggest that  
447 worldwide post-collisional K-rich lavas are generated by melting of metasomatised  
448 phlogopite-bearing garnet-peridotite. The three oldest samples (ASKL-17, ASKL-18,  
449 516-11) exhibit the most mafic major element characteristics in our dataset. They are  
450 distinct, with Sr-Nd isotope compositions slightly less enriched than the younger lavas  
451 of the dataset (Fig. 8). The oldest two samples are also geographically located to the  
452 northwest of the main AVB (Fig. 1). They likely have a slightly different  
453 petrogenetic history, however, we envision a similar process of melting  
454 phlogopite-garnet-bearing SCLM.

455 It is an interesting question as to how such an isotopically homogeneous signature  
456 can be generated from the SCLM, which should be highly heterogeneous given its  
457 long-term enrichment by multiple metasomatic events. Initial metasomatic events of  
458 the Tibetan lithosphere may have begun as early as the Proterozoic when the  
459 Proto-Tethys lithosphere subducted beneath the basement of Tibet, and continued  
460 until the Late Triassic with the closure of Paleo-Tethys Ocean (Jiang et al., 2013;  
461 Mattern and Schneider, 2000; Pullen et al., 2008; Sone and Metcalfe, 2008). The  
462 impacts of Tethyan oceanic lithosphere on Tibetan lithosphere have been

463 demonstrated by several studies of Cenozoic volcanism (e.g., Chung et al., 2005;  
464 Ding et al., 2003).

465 Generally, Nb-Ta-Ti negative anomalies in igneous rocks are indicators of  
466 subduction (Briqueu et al., 1984; Foley et al., 1999). However, contemporary  
467 subduction of the Indian plate is unlikely to result in homogeneous metasomatism of  
468 the entire Tibetan lithosphere (Guo et al., 2006; Turner et al., 1996; Williams et al.,  
469 2004). The metasomatised upper mantle in the plateau is likely to be associated with  
470 slab-derived components such as ancient subducting sediments, which may originate  
471 from Proto-Tethys and Paleo-Tethys oceanic lithospheres.

472 The petrogenesis of AVB discussed above is in accordance with most shoshonites  
473 of the world, such as western Alps (Conticelli et al., 2009), Fiji (Leslie et al., 2009),  
474 Izu-Bonin-Mariana intra-oceanic arc (Ishizuka et al., 2010; Sun and Stern, 2001) and  
475 Aeolian (Peccerillo et al., 2013). They are generally generated by partial melting of an  
476 enriched mantle and display similar geochemical characteristics, including enrichment  
477 in LILE and depletion in Nb-Ta-Ti. However, tectonic mechanisms for partial melting  
478 of enriched mantles are diverse. The majority of shoshonitic magmatism is generated  
479 in three broad tectonic settings (Gill et al., 2004): (1) post-collisional orogens, e.g.  
480 Tibet (Turner et al., 1996) and the Alps (Conticelli et al., 2009); (2) rifting in  
481 continental post-subduction areas and continental magmatic arcs, e.g. Cascades  
482 (Conrey et al., 1997); (3) intra-ocean island arc settings, e.g. Fiji (Leslie et al., 2009)  
483 and Izu-Bonin-Mariana arc (Ishikuka et al., 2010; Sun and Stern, 2001). Shoshonitic  
484 rocks in the former two tectonic settings are mainly characterised by Ce/Yb ratios

485 higher than 46.5 and oceanic-arc related shoshonitic rocks display Ce/Yb ratios lower  
486 than 46.5 (Gill et al., 2004). The Ce/Yb ratios of AVB lavas range from 114 to 191,  
487 which is consistent with the post-collisional settings. Due to the complicated tectonic  
488 setting of the AVB and the multiple possible contributors to their chemical budget  
489 (e.g., subduction package of both Indian and Tarim slabs), a combined geophysical  
490 and geochemical perspective may yield more insight to the triggering mechanism for  
491 partial melting of the enriched SCLM.

492

### 493 *6.3. Integrated Geophysical and Geochemical views*

494 The historic volcanic activity in the AVB allows us to combine present day  
495 seismic images of the region with geochemistry. There are four competing  
496 geodynamical models for the petrogenesis of the volcanism in northwestern Tibet: (1)  
497 convective removal of the lower part of lithosphere (e.g., Chung et al., 2005; Turner et  
498 al., 1993, 1996; Williams et al., 2004; Xia et al., 2011); (2) mixing of Indian and  
499 Tarim mélanges (Guo et al., 2014); (3) addition of subduction components without  
500 mélanges (e.g., Arnaud et al., 1992; Ding et al., 2003; Tapponnier et al., 2001); and (4)  
501 upwelling asthenosphere (Wei et al., 2015, 2016). Here we have the unique  
502 opportunity to investigate which of these scenarios is most consistent with both  
503 geochemical and geophysical constraints.

504

#### 505 *6.3.1. Convective removal of the lower part of lithosphere*

506 Several previous studies highlight the possibility of partial melting of the SCLM

507 by convective removal of the lower part of lithosphere (e.g., Chung et al., 2005;  
508 Cooper et al., 2002; Turner et al., 1993, 1996; Williams et al., 2004; Xia et al., 2011).  
509 According to these geochemical studies, after the primary collision at 50-55 Ma,  
510 under the squeezing pressure of the north-subducting Indian plate and the resisting  
511 Tarim Block, the northwest Tibet lithosphere started to shorten and thicken to twice its  
512 original thickness, accompanied by the fast uplift of the Tibetan Plateau. Subsequently,  
513 owing to gravitational instability and asthenospheric heating, the lower part of the  
514 Tibetan lithosphere was convectively removed. Thinning of the lithosphere led to the  
515 upwelling of asthenosphere, which caused partial melting of the Tibetan SCLM. An  
516 important piece of evidence for this model is that no young volcanism has been found  
517 in southern Tibet after the southern Tibetan lithosphere was underthrust by the cold  
518 Indian Plate at ~10 Ma, which shut down the asthenospheric source (Chung et al.,  
519 2005; Xia et al., 2011).

520 This model can explain the petrogenesis of the K-rich volcanic rocks and their  
521 trace element enrichment. However, it requires the existence of K-rich layer in the  
522 Tibetan lithosphere. Even if it is true, it is still difficult to explain the coincidence of  
523 wide exposure of K-rich volcanism on the whole Tibetan Plateau, which indicates that  
524 volcanism only happens when the lithosphere is thinned to this K-rich layer. In  
525 addition, if the magmatism of AVB is associated with removal of the lower part of  
526 lithosphere, the sinking of the delaminated cold lithosphere would decrease the  
527 temperature of the asthenosphere beneath the AVB. However, tomographic images  
528 (Fig. 2) in this region do not show a fast seismic anomaly expected for delaminated

529 lithosphere, although such a feature could be below the resolution of the seismic  
530 models (~50 km, Wei et al., 2016).

531

### 532 *6.3.2. Mélange melting*

533 As discussed, the mélange model proposed by Guo et al. (2014) is inconsistent  
534 with the radiogenic isotopic homogeneity we document in AVB lavas. The  
535 mélange-melting model is also inconsistent with the following geophysical  
536 observations: (1) Recent seismic results do not support the steep subduction of Indian  
537 plate beneath the AVB (Fig. 2; Tunini et al., 2016; Wei et al., 2015, 2016; Zhao et al.,  
538 2010). Steep subduction of the Indian plate is only observed on the west  
539 (Pamir-Hindu Kush region; Negredo et al., 2007) and east of Tarim basin (south of  
540 Qaidam Basin; Li et al., 2008; Zhao et al., 2010). (2) Because the Indian plate has  
541 subducted more than 600 km beneath the Tibet, it is unclear how the Indian plate is  
542 able to dehydrate and specifically focus volcanism in the AVB.

543

### 544 *6.3.3. Subduction components without mélange assemblages*

545 From south to north, the Tibetan Plateau consists of four roughly  
546 east-west-trending terranes: Lhasa, Qiangtang, Songpan-Ganzi and Kunlun (Dewey,  
547 1988). Tectonic studies suggest that volcanism on the Tibetan Plateau may be  
548 associated with the subduction of Indian and Asian plates (e.g., Arnaud et al., 1992;  
549 Ding et al., 2003; Tapponnier et al., 2001). Specifically, in northwestern Tibet, the  
550 AVB lavas may be generated by the subduction of Indian and Tarim slabs. This

551 subduction model is supported by field observations, such as the East-west-trending  
552 K-rich volcanic belts.

553 However, Cenozoic volcanism on the Tibetan Plateau does not display a pattern  
554 of stepwise subduction of continental lithosphere (e.g., Guo et al., 2006; Williams et  
555 al., 2004). Moreover, this large-scale subduction model is inconsistent with recent  
556 seismic studies. For example, large-scale subduction of Asian lithospheres would  
557 result in an uneven base to the Tibetan lithosphere, which is not observed (Fig. 2; Wei  
558 et al., 2015, 2016; Zhao et al., 2010). Though the existence of the subducting Tarim  
559 Block beneath northwestern Tibet is well-documented (e.g., Wei et al., 2015, 2016;  
560 Wittlinger et al., 2004, Zhao et al., 2010), the impacts of Tarim Block on northwestern  
561 magmatism may be minor, as plate subduction would cause an increase in age of the  
562 northwestern magmatism from north to south, which are not observed (Guo et al.,  
563 2006, 2014).

564

#### 565 *6.3.4. Asthenosphere Upwelling and Shear Heating*

566 Wei et al. (2015; 2016) performed high resolution ( $1^\circ$ ) P-wave velocity  
567 tomography beneath the AVB. They revealed a mantle lithospheric between the Indian  
568 and Tarim slabs directly beneath the AVB, and suggested that the volcanism is  
569 associated with the upwelling of the asthenosphere. These models show that in  
570 northwestern Tibet, the Indian and Tarim LABs are visible in seismic tomography  
571 with fast seismic velocities extending to depths of approximately 250 km (Figure 2),  
572 which is in accordance with the results of Zhao et al. (2010). The upper boundaries

573 between the subducting slabs and Tibetan lithosphere are not observed, suggesting  
574 that the lithosphere of the subducting slabs and the Tibetan lithosphere may have  
575 integrated into one thick lithosphere.

576 However, some lateral variations exist in lithospheric structure. The continuous  
577 fast seismic velocities in the west vertical cross section ( $80^{\circ}\text{E}$ ) of P-wave tomography  
578 indicates that the Indian and Tarim slabs have collided with each other. However, the  
579 middle vertical cross section ( $81.58^{\circ}\text{E}$ , on the AVB) show discontinuous fast seismic  
580 velocities suggesting that the north edge of Indian plate has not yet collided with the  
581 Tarim Block, thus there exists a gap  $\sim 120$  km wide between the two slabs directly  
582 beneath the AVB; the east vertical cross section ( $83^{\circ}\text{E}$ ) shows a larger gap between  
583 those two slabs. This discontinuous lithospheric structure is supported by a recent  
584 joint analysis of seismic velocity, gravity and topography in the Tarim Basin and  
585 surrounding region (Deng et al., 2017) showing that the AVB is underlain by weak,  
586 low-density material compared to the thick, dense and strong Tarim block to the north.  
587 Owing to the limited number of seismic stations in the sparsely populated region, it is  
588 hard to constrain the details of this, but Deng et al. (2017) suggest that the mantle in  
589 this region is anomalously buoyant. They argue that the region is too narrow to be  
590 caused by a thermal anomaly and suggest a compositional anomaly (e.g.,  
591 metamorphism linked to subduction fluids) or a localised heat source (e.g.,  
592 shear-heating) are likely mechanisms to weaken the lithosphere.

593 Global positioning system measurements indicate that the convergence rate  
594 between India and Tarim Basin in the direction of relative motion between India and

595 Eurasia (~N20°E) (Sella et al., 2002) is ~28 mm/year (Zhang et al., 2004). As a result,  
596 the upper mantle in the gap between the Indian and Tarim lithospheres is being  
597 squeezed by the relative motion of the two subducting lithospheres. Since we have  
598 excluded the models of convective removal of the SCLM, subduction and mélange  
599 melting, we speculate that partial melting of the SCLM is likely related to shear  
600 heating and/or upwelling of asthenosphere in the upper mantle. Since a significant  
601 chemical signature of asthenosphere has not been detected in this study, we suggest  
602 that the heat contribution of shear heating may be dominant.

603       Convergence of lithospheres may result in viscous strain-rate melting in the upper  
604 mantle (Kincaid and Silver, 1996), which can provide the heat for partial melting of  
605 the SCLM without removing of the lower part of the SCLM. Furthermore, shear  
606 heating can cause very localised heating in the lithosphere close to large faults  
607 (Leloup et al. 1999) providing a possible explanation for the near invariant radiogenic  
608 isotope signature derived from the SCLM, which should be heterogeneous on a large  
609 scale. The duration of this viscous heating is thought to be short, spanning a period of  
610 ~12-15 Ma (Kincaid and Silver, 1996), which is consistent with the age of  
611 northwestern volcanism (8.27 Ma to present; Cooper et al., 2002; Guo et al., 2016,  
612 2014; Turner et al., 1993; 1996; Williams et al., 2004).

613       Shear heating has been invoked as a mechanism for crustal magmatism, with  
614 recent models suggesting that shear heating coupled with the insulating nature of hot  
615 rocks provides an efficient mechanism for melting in orogenic belts (e.g., Whittington  
616 et al., 2009). For example, leucogranites on an active thrust in the Himalayas have

617 been proposed to result from partial melting triggered by shear-heating (Harrison et al.,  
618 1997, 1998) as well as in other orogens (e.g., Trans-Hudson, Appalachain, Nabalek  
619 and Liu, 2004). In the AVB, the Altyn Tagh fault extends down to a depth of 140 km  
620 with strike-slip shear in the SCLM (Wittlinger et al., 1998), thus it is possible that  
621 shear heating in the SCLM precedes shoshonitic melt generation. Once melts are  
622 formed, the deep-seated lithospheric faults may allow melt to migrate to the Earth  
623 surface, resulting in minimal crustal contamination of the primary magma.

624       If our model that the northwestern volcanism is related to the mantle gap between  
625 the two subducting slabs is correct, the closure of the gap in the west prior to the east  
626 should result in older lavas in the west. As suggested by seismic images (Fig. 2), there  
627 must be a critical point between 80°E and 81.56°E, where the Indian slab has just  
628 collided with the Tarim slab. Tomographic results based on the model of Wei et al.,  
629 (2016) suggest that this critical point is located at ~81°E. To the west of 81°E, the gap  
630 between the two slabs closed prior to the east, thus the volcanism related to the gap  
631 are chronologically older than the volcanism in the east. This chronological difference  
632 is in accordance with the ages of northwestern volcanism summarised by Guo et al.  
633 (2014). To the west of 81°E, the average ages of Tianshuihai, Quanshuigou,  
634 Qitaidaban, Dahongliutan and Kangxiwa lavas are 5.20, 5.23, 8.27, 3.78, 3.24 Ma,  
635 respectively (Fig. 12). In the east of 81°E, the average age of Ashikule, Keliya, Pulu  
636 and Heishibei are 1.07, 0.56, 1.20 and 1.28 Ma, respectively, which are significantly  
637 younger than those of the western volcanic fields (Fig. 12). Additionally, as strong  
638 tectonic activities are usually manifested geomorphologically, we speculate that the

639 formation of arc-shape Kegang fault may also be related to the closure of the  
640 lithospheric gap (Fig. 1, Fig. 12).

641

## 642 7. Summary and Outlook

643 New geochemical analyses of the most recent volcanism in Tibet are combined  
644 with recent tomographic studies beneath the AVB at the northwestern margin of the  
645 Tibetan Plateau. We suggest that AVB lavas are most likely generated by partial  
646 melting of the Tibetan phlogopite-bearing SCLM within the garnet stability field.  
647 While the resolution of the seismic models alone cannot distinguish the mechanism of  
648 heat generation, the homogeneous characteristics of the radiogenic isotope signatures  
649 point to a very localised source. This argues against a broad asthenospheric upwelling  
650 or direct link with subduction-derived fluids or chemically heterogeneous mélange  
651 contributions. Rather, we suggest heat is provided via localised shear-heating along  
652 lithospheric faults accommodating the closure of the Indian and Tarim slabs. This  
653 mechanism, as well as explaining the seismic and radiogenic isotope signatures,  
654 provides a viable means of transport to account for the lack of crustal contamination  
655 in the samples. This model suggests that evolving volcanism in Tibet, and possibly in  
656 other transpressive regimes, are more directly linked to the evolution of large-scale  
657 lithospheric faults as opposed to the subduction of the Indian and Tarim slabs. More  
658 precise dating of tectonic and volcanic activity, more concentrated geochemical study  
659 and improved geophysical imaging are required to fully test this hypothesis.

660

661 Acknowledgements

662 We thank S. Turner and an anonymous reviewer for their constructive comments and  
663 suggestions that helped us greatly to improve the manuscript. We are grateful to B.  
664 Coles and K. Kreissig for their great help of the MAGIC mass spectrometry and  
665 chemistry training. We thank S. Hammond (Open University) for precise trace  
666 element analyses. This work was funded by the National Natural Science Foundation  
667 of China (Grant 41372344) and a China Scholarship Council (CSC) award to FW for  
668 his visit to MAGIC.

669

670 References

671 Arnaud, N.O., Vidal, Ph., Tapponnier, P., Matte, Ph., Deng, W.M., 1992. The high  
672 K<sub>2</sub>O volcanism of northwestern Tibet: Geochemistry and tectonic implications. *Earth  
673 and Planetary Science Letters* 111, 351-367.

674

675 Bie, L., Ryder, I., 2014. Recent seismic and aseismic activity in the Ashikule stepover  
676 zone, NW Tibet. *Geophysical Journal International* 198, 1632-1643.

677

678 Bouvier, A., Vervoort, J.D., Patchett, P.J., 2008. The Lu-Hf and Sm-Nd isotopic  
679 composition of CHUR: Constraints from unequilibrated chondrites and implications  
680 for the bulk composition of terrestrial planets. *Earth and Planetary Science Letters*  
681 273, 48-57.

682

683 Briquieu, L., Bougault, H., Joron, J.L., 1984. Quantification of Nb, Ta, Ti and V  
684 anomalies in magmas associated with subduction zones: petrogenetic implications.  
685 Earth and Planetary Science Letters 68, 297-308.

686

687 Chung, S.L., Chu, M.F., Zhang, Y., Xie, Y., Xie, Y., Lo, C.H., Lee, T.Y., Lan, C.Y., Li,  
688 X., Zhang, Q., Wang, Y., 2005. Tibetan tectonic evolution inferred from spatial and  
689 temporal variation in post-collisional magmatism. Earth Science Reviews 68,  
690 173-196.

691

692 Condamine, P., Medard, E., 2014. Experimental melting of phlogopite-bearing mantle  
693 at 1 GPa: Implication for potassic magmatism. Earth and Planetary Science Letters  
694 397, 80-92.

695

696 Condamine, P., Medard, E., Devidal, J.L., 2016. Experimental melting of  
697 phlogopite-peridotite in the garnet stability field. Contributions to Mineralogy and  
698 Petrology 171, 95.

699

700 Conrey, R.M., Sherrod, D.R., Hooper, P.R., Swanson, D.A., 1997. Diverse primitive  
701 magmas in the Cascade arc, northern Oregon and southern Washington. Canadian  
702 Mineralogist 35, 367-397.

703

704 Conticelli, S., Guarnieri, L., Farinelli, A., Mattei, M., Avanzinelli, R., Bianchini, G.,

705 Boari, E., Tommasini, S., Tiepolo, M., Prelevic, D., Venturelli, G., 2009. Trace  
706 elements and Sr-Nd-Pb isotopes of K-rich, shoshonitic, and calc-alkaline magmatism  
707 of the Western Mediterranean Region: Genesis of ultrapotassic to calc-alkaline  
708 magmatic associations in a post-collisional geodynamic setting. *Lithos* 107, 68-92.

709

710 Cooper, K.M., Reid, M.R., Dunbar, N.W., Mcintosh, W.C., 2002. Origin of mafic  
711 magmas beneath northwestern Tibet: Constraints from  $^{230}\text{Th}$ - $^{238}\text{U}$  disequilibria.  
712 *Geochemistry, Geophysics, Geosystems* 3(11), 1-23.

713

714 Deng, W.M., 1998. *Cenozoic Intraplate Volcanic Rocks in the Northern*  
715 *Qinghai-Xizang Plateau*. Geological Publishing House, Beijing p. 180 (in Chinese  
716 with English abstract).

717

718 Deng, Y., Levandowski, W., & Kusky, T., 2017. Lithospheric density structure  
719 beneath the Tarim basin and surroundings, northwestern China, from the joint  
720 inversion of gravity and topography. *Earth and Planetary Science Letters* 460,  
721 244–254.

722

723 Dewey, J.F., 1988. Extensional collapse of orogens. *Tectonics* 6, 1123-1139.

724

725 Ding, L., Kapp, P., Zhong, D., Deng, W., 2003. Cenozoic volcanism in Tibet:  
726 Evidence for a transition from oceanic to continental subduction. *Journal of Petrology*

727 44(10), 1833-1865.

728

729 Dostal, J., Chatterjee, A.K., 2000. Contrasting behavior of Nb/Ta and Zr/Hf ratios in a  
730 peraluminous granitic pluton (Nova Scotia, Canada). *Chemical Geology* 163,  
731 207-218.

732

733 Elliott, J.R., Walter, R.J., England, P.C., Jackson, J.A., Li, Z., 2010. Parsons, B.,  
734 Extension on the Tibetan plateau: recent normal faulting measured by InSAR and  
735 body wave seismology. *Geophysical Journal International* 183, 503-535.

736

737 Foley, S.F., Barth, M.G., Jenner, G.A., 1999. Rutile/melt partition coefficients for  
738 trace elements and an assessment of the influence of rutile on the trace element  
739 characteristics of subduction zone magmas. *Geochimica et Cosmochimica Acta* 64(5),  
740 933-938.

741

742 Furman, T., Graham, D., 1999. Erosion of lithospheric mantle beneath the East  
743 African Rift system: geochemical evidence from the Kivu volcanic province. *Lithos*  
744 48, 237-262.

745

746 Furuya, M., Yasuda, T., 2011. The 2008 Yutian normal faulting earthquake (Mw 7.1),  
747 NW Tibet: Non-planar fault modelling and implications for the Karakax Fault.  
748 *Tectonophysics* 511(3), 125-133.

749

750 Gill, R.C.O., Aparicio, A., Azzouzi, M.El., Hernandez, J., Thirlwall, M.F., Bourgois, J.,  
751 Marriner, G.F., 2004. Depleted arc volcanism in the Alboran Sea and shoshonitic  
752 volcanism in Morocco: geochemical and isotopic constrains on Neogene tectonic  
753 processes. *Lithos* 78, 363-388.

754

755 Guo. Z., Wilson, M., Liu, J., Mao, Q., 2006. Post-collisional, potassic and  
756 ultrapotassic magmatism of the northern Tibetan Plateau: Constraints on  
757 characteristics of the mantle source, geodynamic setting and uplift mechanisms.  
758 *Journal of Petrology* 47(6), 1177-1220.

759

760 Guo, Z., Wilson, M., Zhang, L., Zhang, M., Cheng, Z., Liu, J., 2014. The role of  
761 subduction channel mélanges and convergent subduction systems in the petrogenesis  
762 of post-collisional K-rich mafic magmatism in NW Tibet. *Lithos* 198-199, 184-201.

763

764 Guo, Z., Wilson, M., Zhang, M., Cheng, Z., Zhang, L., 2015. Post-collisional  
765 ultrapotassic mafic magmatism in south Tibet: Products of partial melting of  
766 pyroxenite in the mantle wedge induced by roll-back and delamination of the  
767 subducted Indian continental lithosphere slab. *Journal of Petrology* 56(7), 1365-1406.

768

769 Hacker, B.R., Ritzwoller, M.H., Xie, J., 2014. Partially melted, mica-bearing crust in  
770 Central Tibet. *Tectonics* 33(7), 1408-1424.

771

772 Harrison, T.M., Lovera O.M., Grove, M., 1997. New insights into the origin of two  
773 contrasting Himalayan granite belts. *Geology* 25(10), 899-902.

774

775 Harrison, T.M., Grove, M., Lovera O.M., Caltos, E.J., 1998. A model for the origin of  
776 Himalayan anataxis and inverted metamorphism. *Journal of Geophysical Research*  
777 103(B11), 27017-27032.

778

779 Huang, F., Chen, J.L., Xu, J.F., Wang, B.D., Li, J., 2015. Os-Nd-Sr isotopes in  
780 Miocene ultrapotassic rocks of southern Tibet: Partial melting of a pyroxenite-bearing  
781 lithospheric mantle. *Geochimica et Cosmochimica Acta* 163, 279-298.

782

783 Ishizuka, O., Yuasa, M., Tamura, Y., Shukuno, H., Stern, R.J., Naka, J., Joshima, M.,  
784 Taylor, R.N., 2010. Migrating shoshonitic Magmatism tracks Izu-Bonin-Mariana  
785 intra-oceanic arc rift propagation. *Earth and Planetary Science Letters* 294, 111-122.

786

787 Jackson, M.G., Hart, S.R., Kopperss, A.P., Staudigel, H., Konter, J., Blusztajn, J.,  
788 Kurz, M., Russell, J., 2007. The return of subducted continental crust in Samoan lavas.  
789 *Nature* 448, 684-687.

790

791 Jiang, Y.H., Jia, R.Y., Liu, Z., Liao, S.Y., Zhao, P., Zhou, Q., 2013. Origin of Middle  
792 Trissic high-K calc-alkaline granitoids and their potassic microgranular enclaves from

793 the western Kunlun orogeny, northwest China: A record of the closure of Paleo-Tethys.  
794 *Lithos* 156-159, 13-30.

795

796 Kalfoun, F., Ionov, D., Merlet, C., 2002. HFSE residence and Nb/Ta ratios in  
797 metasomatised, rutile-bearing mantle peridotites. *Earth and Planetary Science Letters*  
798 199, 49-65.

799

800 Kincaid, C., Silver, P., 1996. The role of viscous dissipation in the orogenic process.  
801 *Earth and Planetary Science Letters* 142, 271-288.

802

803 Kushiro, I., Syono, Y., Akimoto, S.I., 1968. Stability of phlogopite at high pressures  
804 and possible presence of phlogopite in the Earth's upper mantle. *Earth and Planetary*  
805 *Science Letters* 3, 197-203.

806

807 Kutzbach, J.E., Prell, W.L., Ruddiman, W.F., 1993. Sensitivity of Eurasian climate to  
808 surface uplift of the Tibetan Plateau. *The Journal of Geology* 101, 177-190.

809

810 Le Bas, M.J., Le Maitre, L.E., Streckeisen, A., Zanettin, B., 1986. A chemical  
811 classification of volcanic rocks based on the total alkali-silica diagram. *Journal of*  
812 *Petrology* 27(3), 745-750.

813

814 Leloup, P. H., Ricard, Y., Battaglia, J. and Lacassin, R., 1999. Shear heating in

815 continental strike-slip shear zones: model and field examples. *Geophysical Journal*  
816 *International*, 136, 19-40.

817

818 Leslie, R.A.J., Danyushevsky, L.V., Crawford, A.J., Verbeeten, A.C., 2009. Primitive  
819 shoshonites from Fiji: Geochemistry and source components. *Geochemistry,*  
820 *Geophysics, Geosystems* 10(7).

821

822 Li, C., van der Hilst, R.D., Meltzer, A.S., Engdahl, E.R., 2008. Subduction of the  
823 Indian lithosphere beneath the Tibetan Plateau. *Earth and Planetary Science Letters*  
824 274, 157-168.

825

826 Li, H.B., Yang, J.S., Xu, Z.Q., Sun, Z.M., Tapponnier, P., van der Woerd, J., Meriaux,  
827 A.S., 2006. The constraint of the Altyn Tagh fault system to the growth and rise of the  
828 northern Tibetan plateau, *Earth Science Frontiers* 13(4), 59-79 (in Chinese with  
829 English Abstract).

830

831 Liu, J., Maimaiti, Y., 1989. Distribution and ages of Ashikule volcanoes on the West  
832 Kunlun Mountains, west China. *Bulletin of Glacier Research* 7, 187-190.

833

834 Marschall, H.R., Schumacher, J.C., 2012. Arc magmas sourced from mélange dispirs  
835 in subduction zones. *Nature Geoscience* 5, 862-867.

836

837 Mattern, F., Schneider, W., 2000. Suturing of the Proto- and Paleo-Tethys oceans in  
838 the western Kunlun (Xinjiang, China). *Journal of Asian Earth Sciences* 18, 637-650.

839

840 Miller, C., Schuster, R., Klotzli, U., Frank, W., Purtscheller, F., 1999. Post-collisional  
841 Potassic and ultrapotassic magmatism in SW Tibet: Geochemical and Sr-Nd-Pb-O  
842 isotopic constraints for mantle source characteristics and petrogenesis. *Journal of*  
843 *Petrology* 40(9), 1399-1424.

844

845 Mo, X., Zhao, Z., Deng, J., Flower, M., Yu, X., Luo, Z., Li, Y., Zhou, S., Dong, G.,  
846 Zhu, D., Wang, L., 2006. Petrology and geochemistry of postcollisional volcanic  
847 rocks from the Tibetan plateau: Implications for lithosphere heterogeneity and  
848 collision-induced asthenospheric mantle flow. *Geological Society of America Special*  
849 *Papers* 409: 507-530.

850

851 Nabelek, P.I., Liu, M., 2004. Petrologic and thermal constraints on the origin of  
852 leucogranites in collisional orogens. *Geological Society of America Special Papers*  
853 398, 73-85.

854

855 Negredo, A.M., Replumaz, A., Villasenor, A., Guillot, S., 2007. Modeling the  
856 evolution of continental subduction processes in the Pamir-Hindu Kush region. *Earth*  
857 *and Planetary Science Letters* 259, 212-225.

858

859 Peccerillo, A., De Astis, G., Faraone, D., Forni, F., Frezzotti, M.L., 2013.  
860 Compositional variations of magmas in the Aeolian arc: implications for petrogenesis  
861 and geodynamics. Geological Society, London, Memoirs 37, 491-510.  
862

863 Plank, T., Langmuir, C.H., 1998. The chemical composition of subducting sediment  
864 and its consequences for the crust and mantle. Chemical Geology 145, 325-394.  
865

866 Pullen, A., Kapp, P., Gehrels, G.E., Vervoort, J.D., Ding, L., 2008. Triassic continental  
867 subduction in central Tibet and Mediterranean-style closure of the Paleo-Tethys  
868 Ocean. Geology 36(5), 351-354.  
869

870 Royden, L.H., Burchfiel, B.C., van der Hilst, R.D., 2008. The geological evolution of  
871 the Tibetan Plateau. Science 321, 1054-1058.  
872

873 Rudnick, R.L., Gao, S., 2003. In *The Crust* 1-64, Vol. 3 of *Treatise in Geochemistry*  
874 (Elsevier, Amsterdam, 2003).  
875

876 Sella, G.F, Dixon, T.H., Mao, A., 2002. REVEL: A model for recent plate velocities  
877 from space geodesy. Journal of Geophysical Research 107(B4), 2081.  
878

879 Sone, M., Metcalfe, I., 2008. Parallel Tethyan sutures in mainland Southeast Asia:  
880 New insights for Palaeo-Tethys closure and implications for the Indosinian orogeny.

881 Comptes Rendus Geoscience 340(2), 166-179.

882

883 Sudo, A., Tatsumi, Y., 1990. Phlogopite and K-amphibole in the upper mantle:  
884 Implication for magma genesis in subduction zones. Geophysical Research Letters  
885 17(1), 29-32.

886

887 Sun, S.S., McDonough, W.F., 1989. Chemical and isotopic systematics of oceanic  
888 basalts: implications for mantle composition and processes. Geological Society,  
889 London, Special Publications 42, 313-345.

890

891 Sun, C.H., Stern, R.J., 2001. Genesis of Mariana shoshonites: Contribution of the  
892 subduction component. Journal of Geophysical Research 106(B1), 589-608.

893

894 Tanaka, T., Togashi, S., Kamioka, H., Amakawa, H., Kagami, H., Hamamoto, T.,  
895 Yuhara, M., Orihashi, Y., Yoneda, S., Shimizu, H., Kunimaru, T., Takahashi, K.,  
896 Yanagi, T., Nakano, T., Fujimaki, H., Shinjo, R., Asahara, Y., Tanimizu, M.,  
897 Dragusanu, C., 2000. JNdi-1: a neodymium isotopic reference in consistency with  
898 LaJolla neodymium. Chemical Geology 168, 279-281.

899

900 Tapponnier, P., Zhiqin, X., Roger, F., Meyer, B., Arnaud, N., Wittlinger, G., Jingsui, Y.,  
901 2001. Oblique stepwise rise and growth of the Tibet Plateau. Science 294, 1671-1677.

902

903 Thirlwall, M.F., 1991. Long-term reproducibility of multicollector Sr and Nd isotope  
904 ratio analysis. *Chemical Geology* 94, 85-104.

905

906 Tunini, L., Jimenez-Munt, I., Fernandez, M., Verges, J., Villasenor, A., Melchiorre, M.,  
907 Afonso, J.C., 2016. Geophysical-petrological model of the crust and upper mantle in  
908 the India-Eurasia collision zone. *Tectonics* 35(7), 1642-1669.

909

910 Turner, S., Arnaud, N., Liu, J., Rogers, N., Hawkesworth, C., Harris, N., Kelley, S.,  
911 van Calsteren, P., Deng, W., 1996. Post-collision, shoshonitic volcanism on the  
912 Tibetan Plateau: Implications for convective Thinning of the Lithosphere and the  
913 source of ocean island basalts. *Journal of Petrology* 37, 45-71.

914

915 Turner, S., Hawkesworth, C., Liu, J., Rogers, N., Kelley, S., van Clasteren, P., 1993.  
916 Timing of Tibetan uplift constrained by analysis of volcanic rocks. *Nature* 364, 50-54.

917

918 Wang, E., Wan, J., Liu, J., 2003. Late Cenozoic geological evolution of the foreland  
919 basin bordering the West Kunlun range in Pulu area: Constraints on timing of uplift of  
920 northern margin of the Tibetan Plateau. *Journal of Geophysical Research: Solid Earth*  
921 108, B8.

922

923 Wang, Q., McDemott, F., Bollon, H., Zhu, Y.T., 2005. Cenozoic K-rich adakitic  
924 volcanic rocks in the Hohxil area, northern Tibet: Lower-crustal melting in an

925 intracontinental setting. *Geology* 33(6), 465-468.

926

927 Wang, Q., Hawkesworth, C.J., Wyman, D., Chung, S.L., Wu, F.Y., Li, X.H., Li, Z.X.,  
928 Guo, G.N., Zhang, X.Z., Tang, G.J., Dan, W., Ma, L., Dong, Y.H., 2016.  
929 Pliocene-Quaternary crustal melting in central and northern Tibet and insights into  
930 crustal flow. *Nature Communications* 7, 11888.

931

932 Wang, Z., 2004. Tectonic evolution of the western Kunlun orogenic belt, western  
933 China. *Journal of Asian Earth Sciences* 24, 153-161.

934

935 Wei, W., Xu, J., Yu, H., Wei, F., 2015. Origin of the Ashi volcano, Western Kunlun  
936 Mountains: Evidence from seismic tomography. *Earth Science Frontiers* 6, 227-232  
937 (In Chinese with English Abstract).

938

939 Wei, W., Zhao, D., Xu, J., Zhou, B., Shi, Y., 2016. Depth variation of P-wave  
940 azimuthal anisotropy beneath Mainland China. *Scientific Reports* 6: 29614.

941

942 Weis, D., Frey, F.A., 1991. Isotope geochemistry of the Ninetyeast Ridge basement  
943 basalts: Sr, Nd, and Pb evidence for involvement of the Kerguelen hot spot. *Proc.*  
944 *Ocean Drill Program Sci. Results* 121, 591-610.

945

946 Weis, D., Frey, F.A., 1996. Role of the Kerguelan Plume in generating the eastern

947 India Ocean seafloor. *Journal of Geophysics Research: Solid Earth* 101(B6),  
948 13831-13849.

949

950 Weyer, S., Munker, C., Mezger, K., 2003. Na/Ta, Zr/Hf and REE in the depleted  
951 mantle: implications for the differentiation history of the crust-mantle system. *Earth  
952 and Planetary Science Letter* 205, 309-324.

953

954 White, W.M., 2015. Probing the earth's deep interior through geochemistry.  
955 *Geochemical Perspectives* 4(2), 95-250.

956

957 Whittington A.G., Hofmeister A.M., Nabelek, P.I., 2009. Temperature-dependent  
958 thermal diffusivity of the Earth's crust and implications for magmatism. *Nature* 458,  
959 319-321.

960

961 Williams, H.M., Turner, S.P., Pearce, J.A., Kelley, S.P., Harris, N.B.W., 2004. Nature  
962 of the source regions for post-collisional, potassic magmatism in southern and  
963 northern Tibet from Geochemical variations and inverse trace element modelling.  
964 *Journal of Petrology* 45(3), 555-607.

965

966 Wittlinger, G., Tapponnier, P., Poupinet, G., Mei, J., Danian S., Herquel, G., Masson,  
967 F., 1998. Tomographic evidence for localized lithospheric shear along the Altyn Tagh  
968 fault. *Science* 282, 74-76.

969

970 Wittlinger, G., Vergne, J., Tapponnier, P., Farra, V., Poupinet, G., Jing, M., Su, H.,  
971 Herquel, G., Paul, A., 2004. Teleseismic imaging of subducting lithosphere and Moho  
972 offsets beneath western Tibet. *Earth and Planetary Science Letters* 221, 117-130.

973

974 Wyllie, P.J., Sekine, T., 1982. The formation of mantle phlogopite in subduction zone  
975 hybridization. *Contributions to Mineralogy and Petrology* 79(4), 375-380.

976

977 Xia, L., Li, X., Ma, Z., Xu, X., Xia, Z., 2011. Cenozoic volcanism and tectonic  
978 evolution of the Tibetan plateau. *Gondwana Research* 19, 850-866.

979

980 Xu, J., Zhao, B., Zhang, L., Chen, Z., 2012. Field geological exploration of the  
981 Ashikule Volcano Group in Western Kunlun Mountains. *Earthquake Research in*  
982 *China* 26(2), 152-159.

983

984 Xu, J., Zhao, B., Sindney, H., Chen, Z.Q., Zhang, L.Y., 2014. Geological features and  
985 eruption history of Ashikule volcano clusters in western Kunlun Mountain. *Acta*  
986 *Petrological Sinica*, 30(12), 3521-3530 (in Chinese with English Abstract).

987

988 Xu, X., Tan, X., Yu, G., Wu, G., Fang, W., Chen, J., Song, H., Shen, J., 2013. Normal-  
989 and oblique-slip of the 2008 Yutian earthquake: Evidence for eastward block motion,  
990 northern Tibetan Plateau. *Tectonophysics* 584, 152-165.

991

992 Yang, J.H., Chung, S.L., Zhai, M.G., Zhou, X.H., 2004. Geochemical and Sr-Nd-Pb  
993 isotopic compositions of mafic dikes from Jiaodong Peninsula, China: evidence for  
994 vein-plus-peridotite melting in the lithospheric mantle. *Lithos* 73, 145-160.

995

996 Yu, H., Xu, J., Zhao, B., Shen, H., Lin, C., 2014. Magmatic processes of Ashi Volcano,  
997 western Kunlun Mountains, China. *Acta Geologica Sinica (English Edition)* 88(2),  
998 530-543.

999

1000 Zhang, P.Z., Shen, Z, Wang, M., Gan, W., Burgmann, R., Molnar, P., Wang, Q., Niu,  
1001 Z., Sun, J., Wu, J., Hanrong, S., Xinzhao, Y., 2004. Continuous deformation of the  
1002 Tibetan Plateau from global positioning system data. *Geology* 32(9), 809-812.

1003

1004 Zhao, J., Yuan, X., Liu, H., Kumar, P., Pei, S., Kind, R., Zhang, Z., Teng, J., Ding, L.,  
1005 Gao, X., Xu, Q., Wang, W., 2010. The boundary between the Indian and Asian  
1006 tectonic plates below Tibet. *Proceedings of the National Academy of Sciences*,  
1007 107(25), 11229-11233.

1008

1009 Zhisheng, A., Kutzbach, J.E., Prell, W.L., Porter, S.C., 2001. Evolution of Asian  
1010 monsoons and phased uplift of the Himalaya-Tibetan plateau since Late Miocene  
1011 times. *Nature* 411, 62-66.

1012

1013 Zindler, A., Hart, S., 1986. Chemical geodynamics. *Annual Review of Earth and*  
1014 *Planetary Sciences* 14, 493-571.

1015

## 1016 Figure Captions

1017 Fig. 1. (a) Tectonic map of the northwest margin of the Tibetan Plateau, modified  
1018 after Furuya and Yasuda (2011), Xu et al. (2013) and Bie and Ryder (2014). Black,  
1019 green and red focal mechanisms represent the main shocks of the 2008, 2012 and  
1020 2014 earthquakes, respectively, according to the Global Centroid-Moment-Tensor  
1021 (CMT) catalog. (b) Geological map of the Ashikule volcanic basin (AVB), modified  
1022 after Liu and Maimaiti (1989) and Xu et al. (2012). Red arrows represent the direction  
1023 of the lava flow. Black open circles represent the location of lava samples, and the ID  
1024 of samples is also marked with a black arrow. Locations of main volcanoes in the  
1025 AVB are marked with red triangles. AS: Ashi Volcano; DH: Dahei Volcano; XS:  
1026 Xishan Volcano; MT: Mati Volcano; DS: Dong volcano; HL: Heilong Volcano; MN:  
1027 Maoniu Volcano; YY: Yueya Volcano; MG: Migong Volcano; WL: Wuluke Volcano;  
1028 YZ: Yizi Volcano; GT: Gaotai Volcano; BH: Binhu Volcano; YS: Yin Volcano.

1029 Fig. 2. Vertical cross sections of P-wave anisotropy tomography (isotropic velocities  
1030 only are shown) along 3 profiles shown on the inset map (see Wei et al., 2016 for  
1031 details of the method). (a) Vertical cross section of 80°E suggests that the Indian slab  
1032 has collided with the Tarim slab. (b) Vertical cross section of 81.53°E (on the AVB)  
1033 suggests that there is a small gap between the two slab beneath the AVB. (c) Vertical  
1034 cross section of 83°E displays a wider gap between the two slabs.

1035 Fig. 3. Photomicrographs of four representative volcanic rocks in the AVB under  
1036 cross-polarised light. Cpx, clinopyroxene; Opx, orthopyroxene; Phl, phlogopite; Pl,  
1037 plagioclase. (a) Sample ASKL-5. Phenocrysts of orthopyroxene and plagioclase  
1038 showing disequilibrium textures including extensive embayments. (b) Sample 513-11.  
1039 Phenocrysts of clinopyroxene, plagioclase and phlogopite in a highly vesicular matrix.  
1040 (c) Sample ASKL-12. A large plagioclase glomerocryst in a crystalline matrix. (d)  
1041 Sample 518-9. Phenocrysts of clinopyroxene, plagioclase and orthopyroxene in a  
1042 porphyritic texture.

1043 Fig. 4. Classification for lava samples in the AVB: (a) SiO<sub>2</sub> versus Na<sub>2</sub>O + K<sub>2</sub>O (wt%),  
1044 (b) Na<sub>2</sub>O versus K<sub>2</sub>O (wt%). The boundaries of diagram (a) and (b) are from Le Bas  
1045 et al. (1986) and Miller et al. (1999), respectively.

1046 Fig. 5. Major element variation diagrams for the studied samples in AVB. Symbols  
1047 are as in Fig. 2. The most recent lava sample (ASKL-3) is marked with a cross inside  
1048 the circle.

1049 Fig. 6. Primitive mantle-normalized trace element (a) and chondrite-normalized rare  
1050 earth element patterns (b) for AVB lavas. Primitive mantle and chondrite  
1051 normalization values are from Sun and McDonough (1989). EMII (Samoa) (Jackson  
1052 et al., 2007), globally subducting sediment (GLOSS; Plank and Langmuir, 1998) and  
1053 upper continental crust (UCC, Rudnick and Gao, 2003) compositions are presented  
1054 for comparison.

1055 Fig. 7. (a) Primitive mantle-normalized La/Yb ratios ((La/Yb)<sub>n</sub>) versus MgO (wt%);  
1056 (b) (La/Yb)<sub>n</sub> versus La (ppm). (c) Eu anomaly (Eu/Eu\*) versus MgO (wt%); Eu/Eu\*

1057 =  $Eu_n \times 2 / (Sm_n + Gd_n)$ ;  $Eu_n$ ,  $Sm_n$  and  $Gd_n$  are the primitive mantle-normalized Eu,  
1058 Sm and Gd concentrations of studied sample, respectively. (d) Ti anomaly ( $Ti/Ti^*$ )  
1059 versus  $SiO_2$  (wt%);  $Ti/Ti^* = Ti_n \times 2 / (Eu_n + Tb_n)$ ;  $Ti_n$  and  $Tb_n$  are the primitive mantle  
1060 –normalized Ti and Tb, respectively. (e) Ba/Th ratios versus Th/Nd ratios. (f) Th/La  
1061 ratios versus Sm/La ratios. Symbols are as in Fig. 2.

1062 Fig. 8. Present day  $^{87}Sr/^{86}Sr$  versus  $^{143}Nd/^{144}Nd$  for lavas from the AVB. Literature  
1063 data specifically from the AVB are presented for comparison (Cooper et al., 2002;  
1064 Guo et al., 2006, 2014; Williams et al., 2004). Enriched mantles (EM I, EM II), bulk  
1065 silicate earth (BSE), Indian and Pacific MORB fields are modified from Zindler and  
1066 Hard (1986) and White (2015).

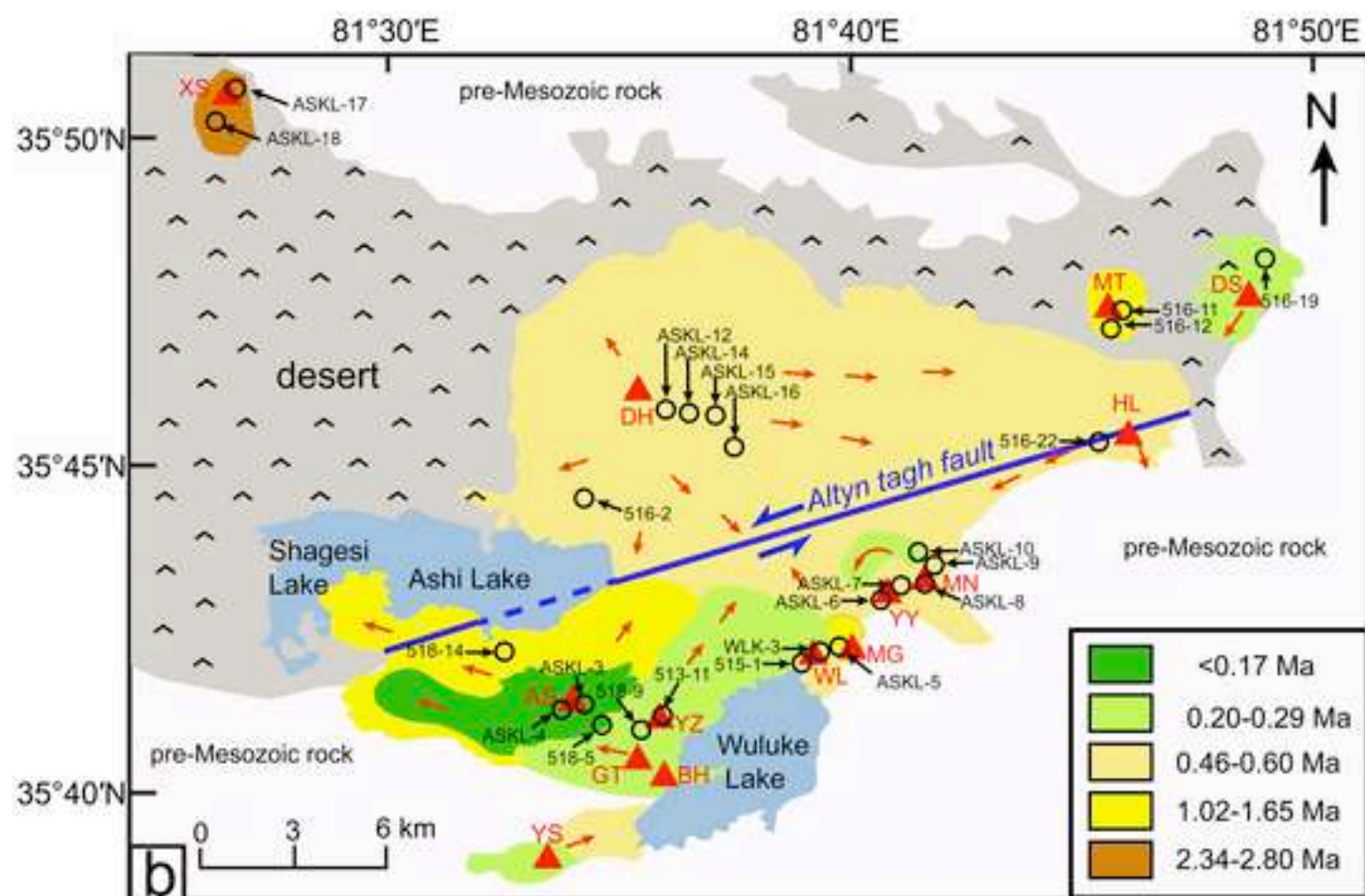
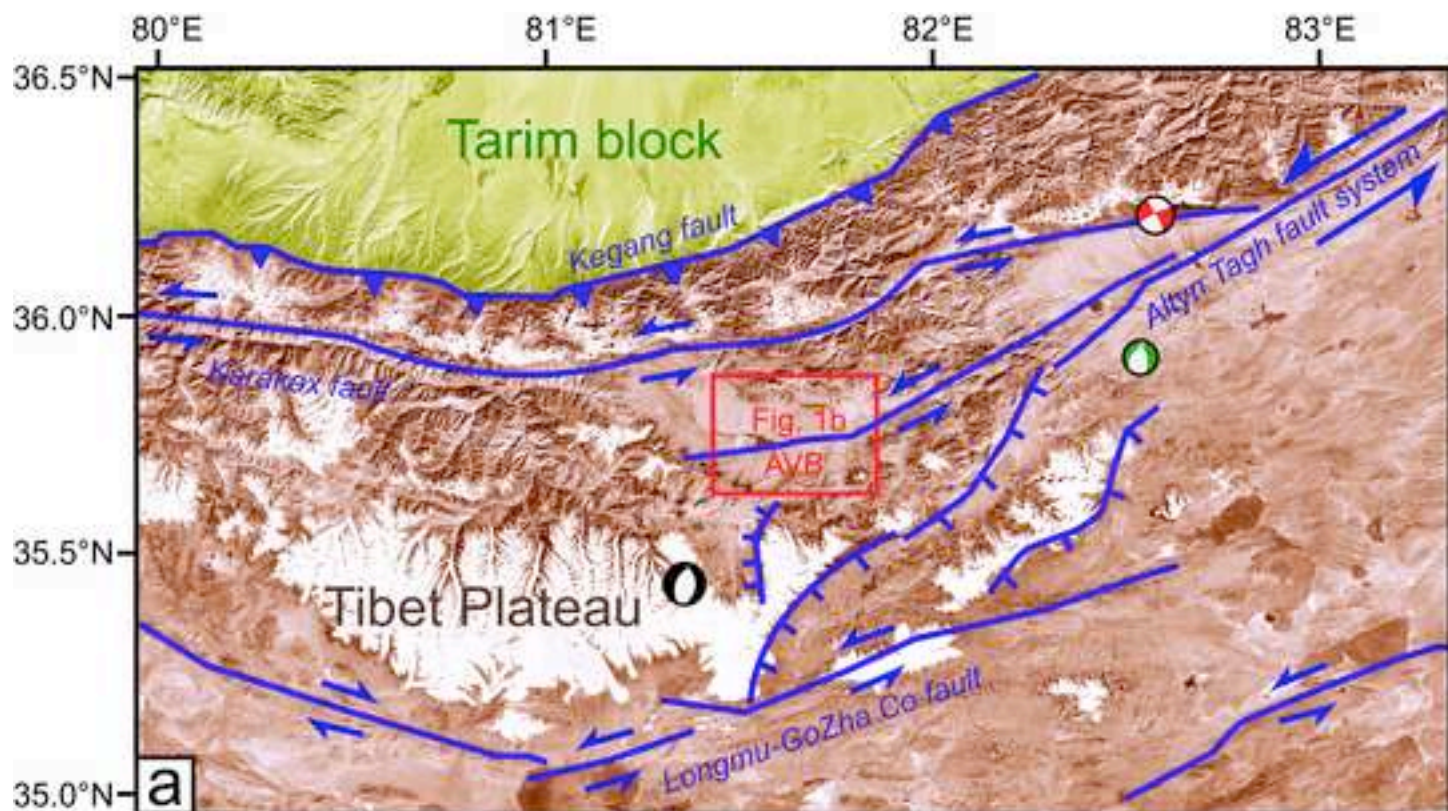
1067 Fig. 9.  $SiO_2$  versus  $^{87}Sr/^{86}Sr$  (a) and  $^{143}Nd/^{144}Nd$  ratios (b) for the AVB lavas. Symbols  
1068 as in Figure 2.

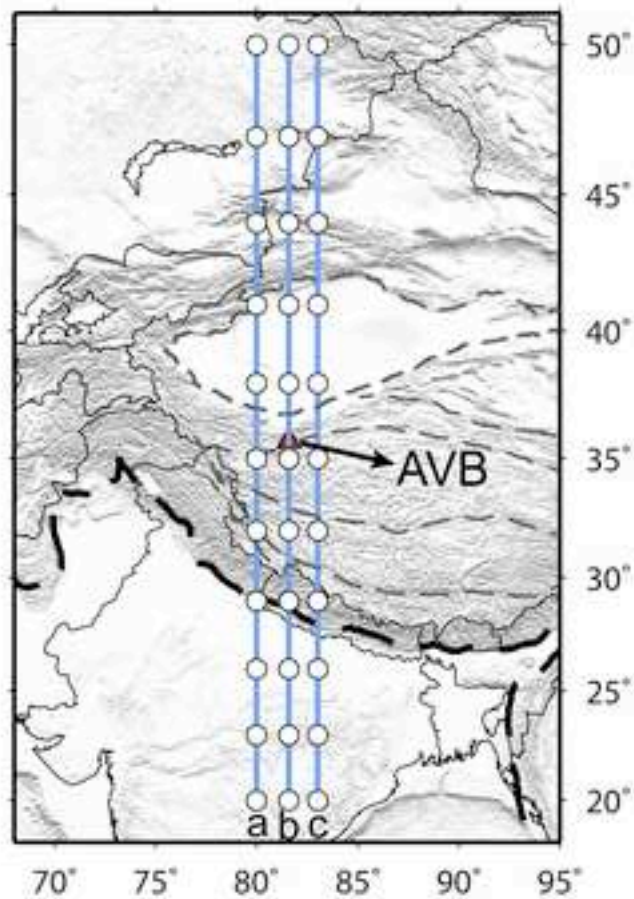
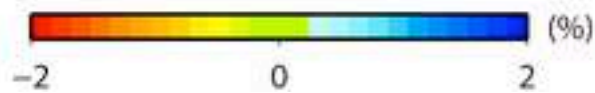
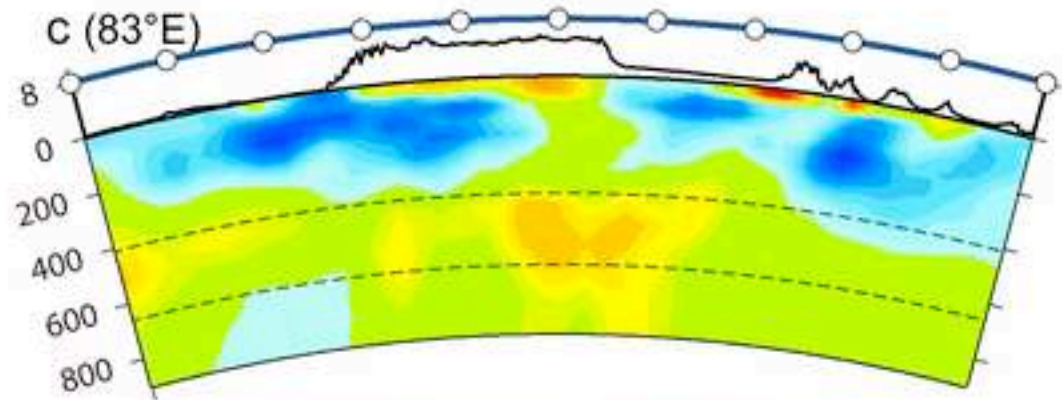
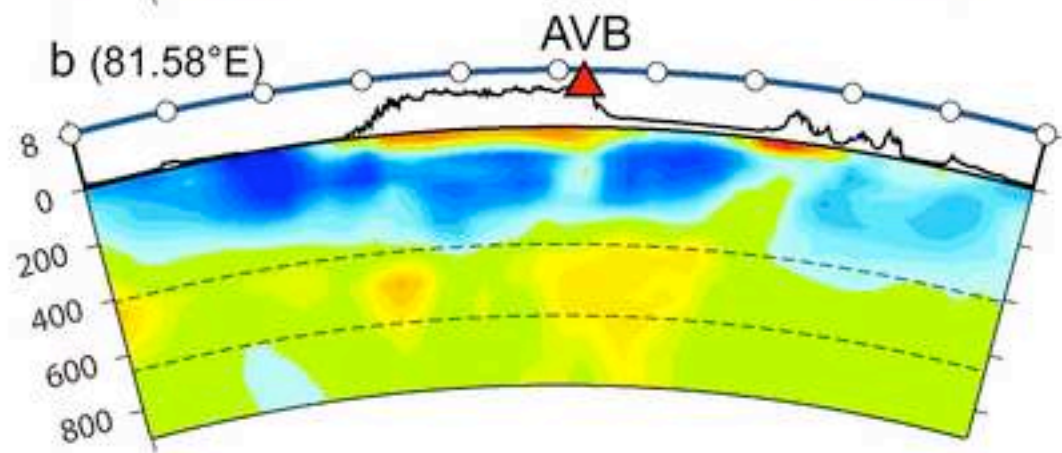
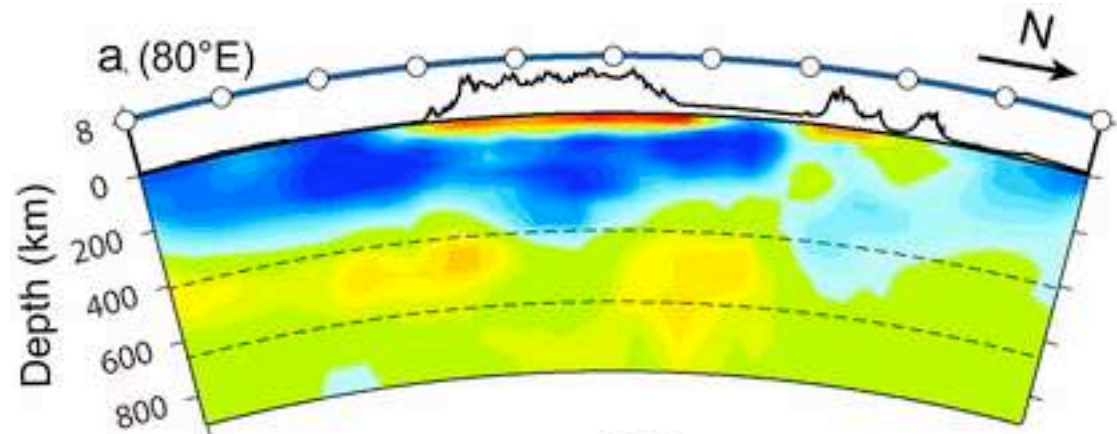
1069 Fig. 10. Zr/Hf versus Nb/Ta ratios of the AVB lavas. Plots of upper continental crust  
1070 (UCC; Rudnick and Gao, 2003), primitive mantle (PM; Sun and McDonough, 1989),  
1071 global subducting sediments (GLOSS; Plank and Langmuir, 1998) and EM II Samoan  
1072 source (Jackson et al., 2007) are displayed for comparison.

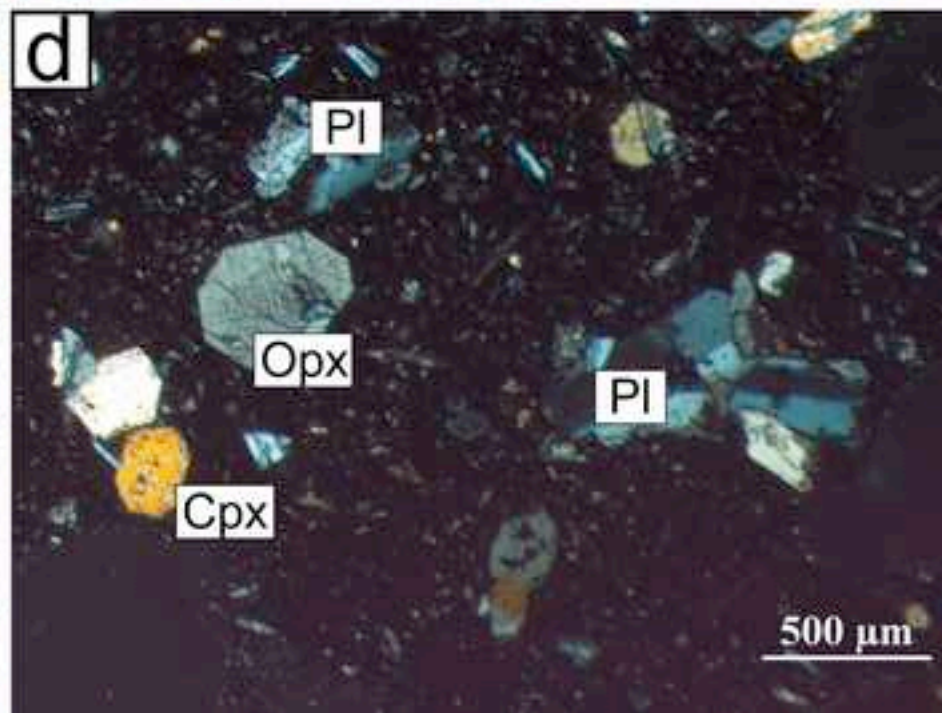
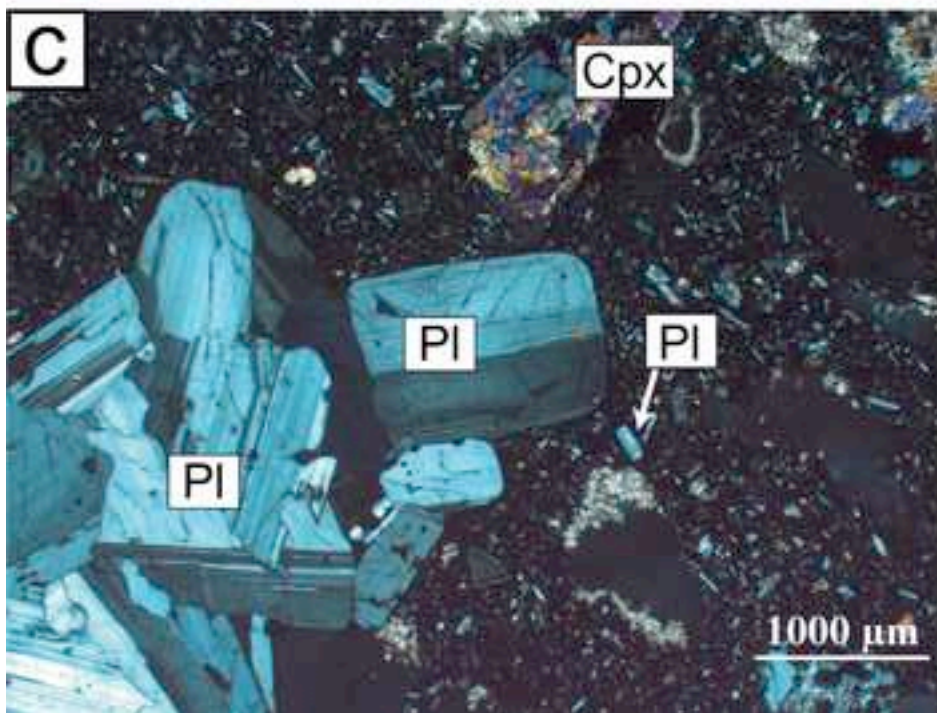
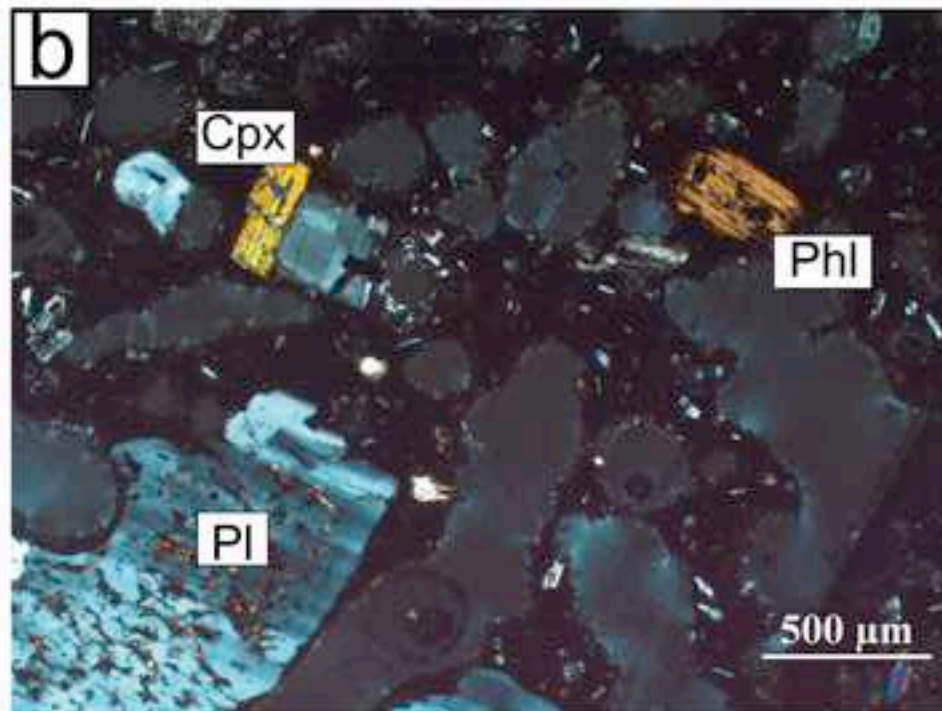
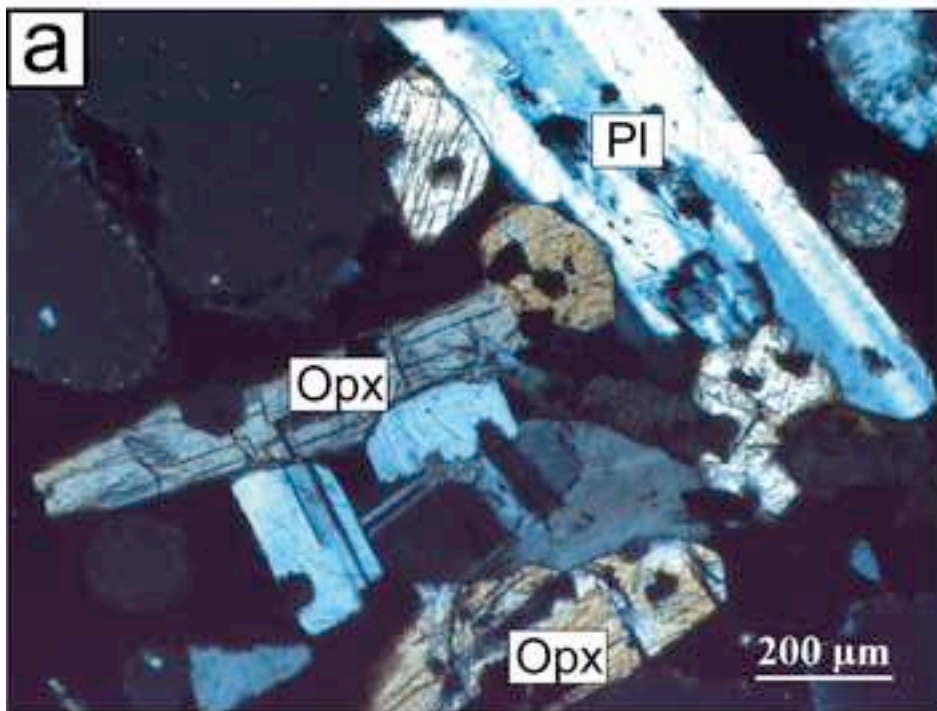
1073 Fig. 11. Rb/Sr versus Ba/Rb for the AVB lavas (after Furman and Graham, 1999). The  
1074 field of common lithospheric mantle (CLM) is taken from Furman and Graham  
1075 (1999).

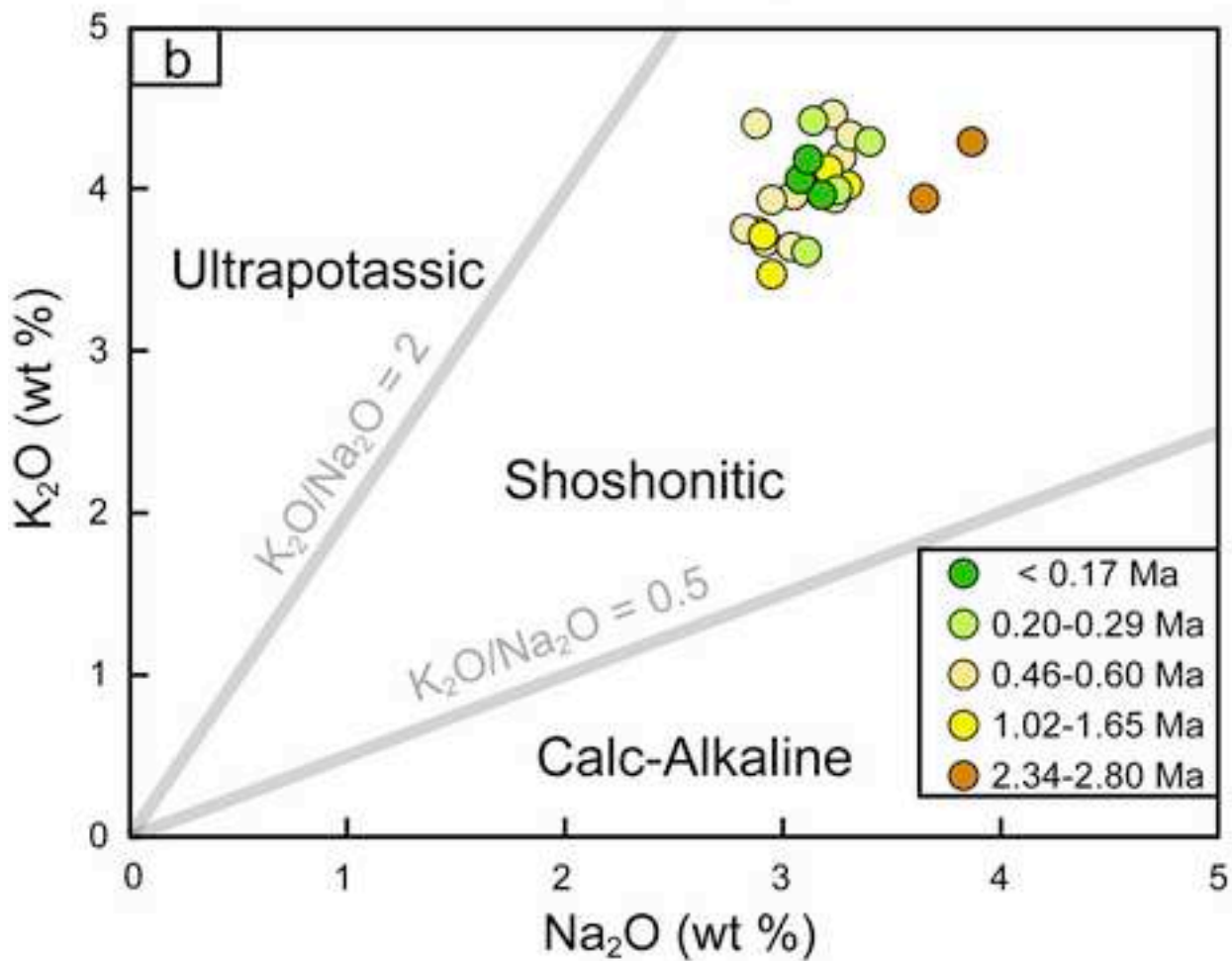
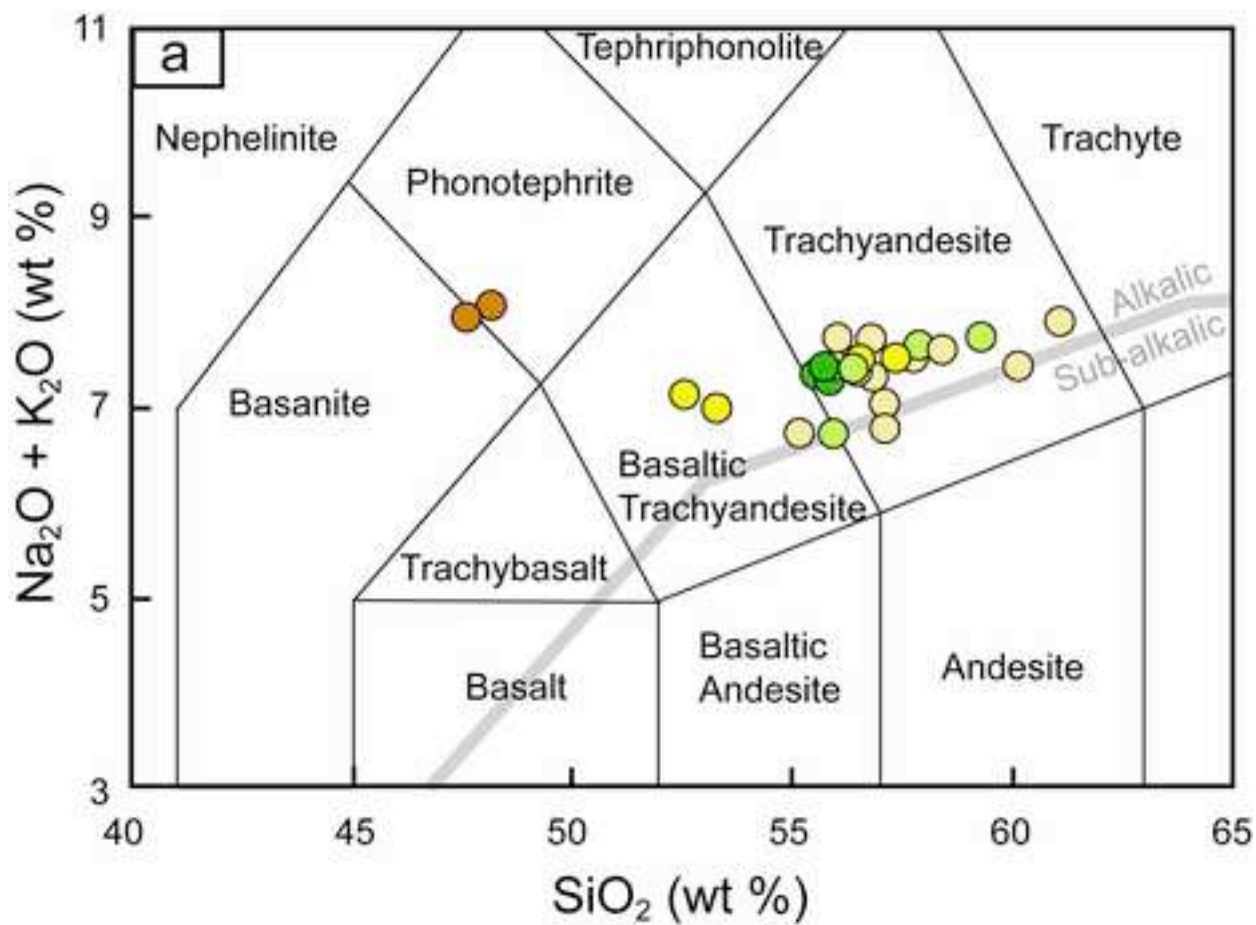
1076 Fig. 12. Schematic model for the post-collisional magmatism in northwestern Tibet  
1077 and lithospheric sections of the present settings. The locations and average ages of the  
1078 volcanic fields are modified from Guo et al. (2014). In the section of  $79^\circ E$ , Indian and

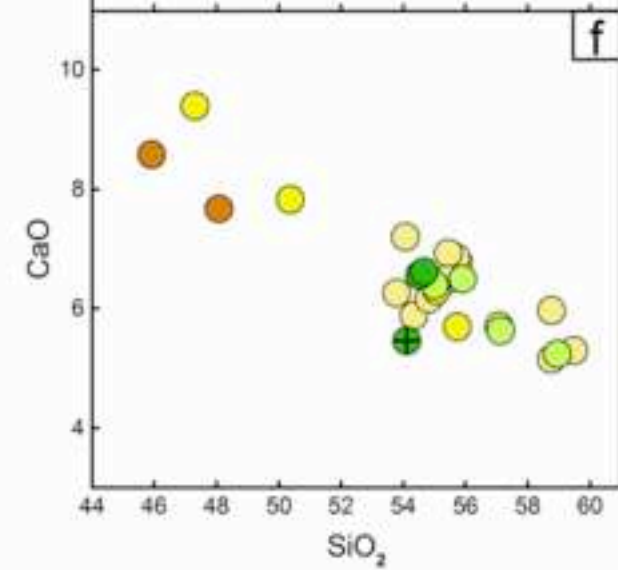
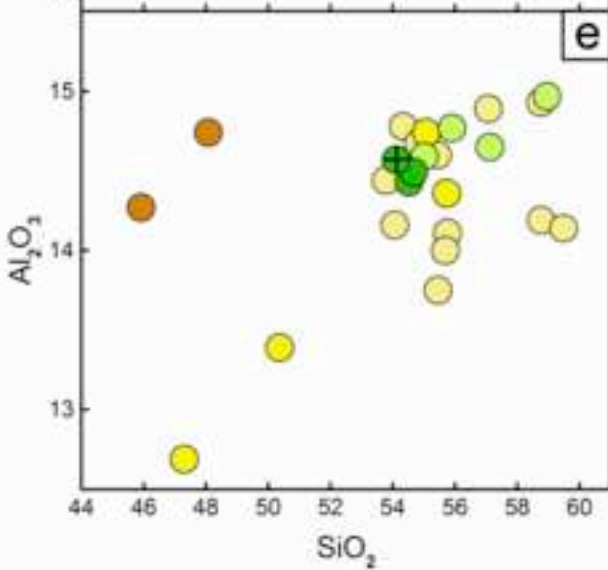
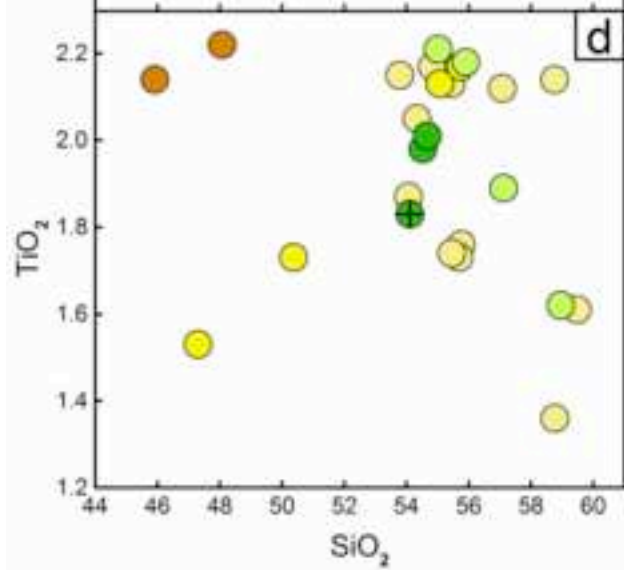
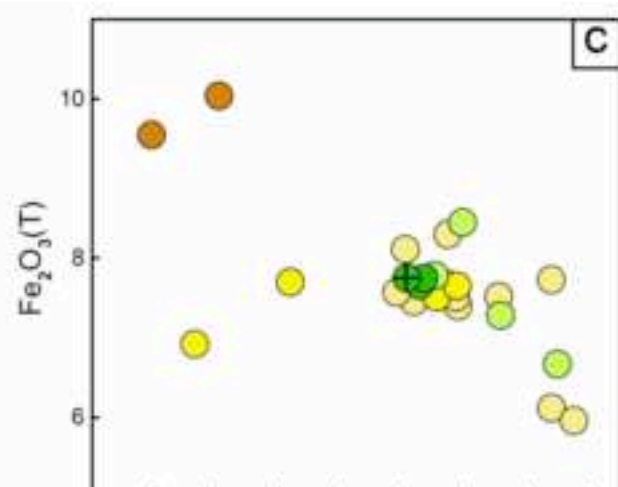
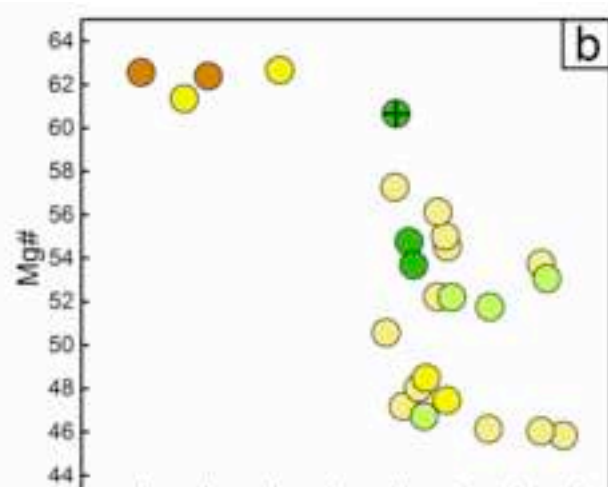
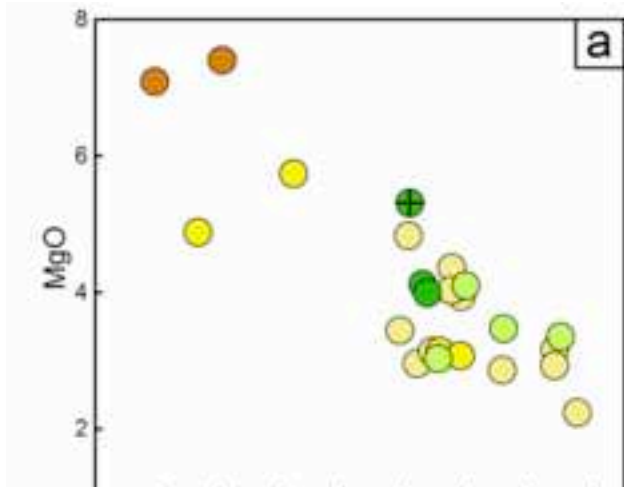
1079 Tarim lithospheres have collided together beneath the west Kunlun Mountains. In the  
1080 section of 81°E, the two slabs just collide together. In the section of 83°E, there is a  
1081 gap between the Indian and Tarim lithospheres. The progressive closure of this gap  
1082 may lead to shear heating, melting of the Tibetan SCLM and focussing of magmatism  
1083 with transport along deep-seated lithospheric faults.

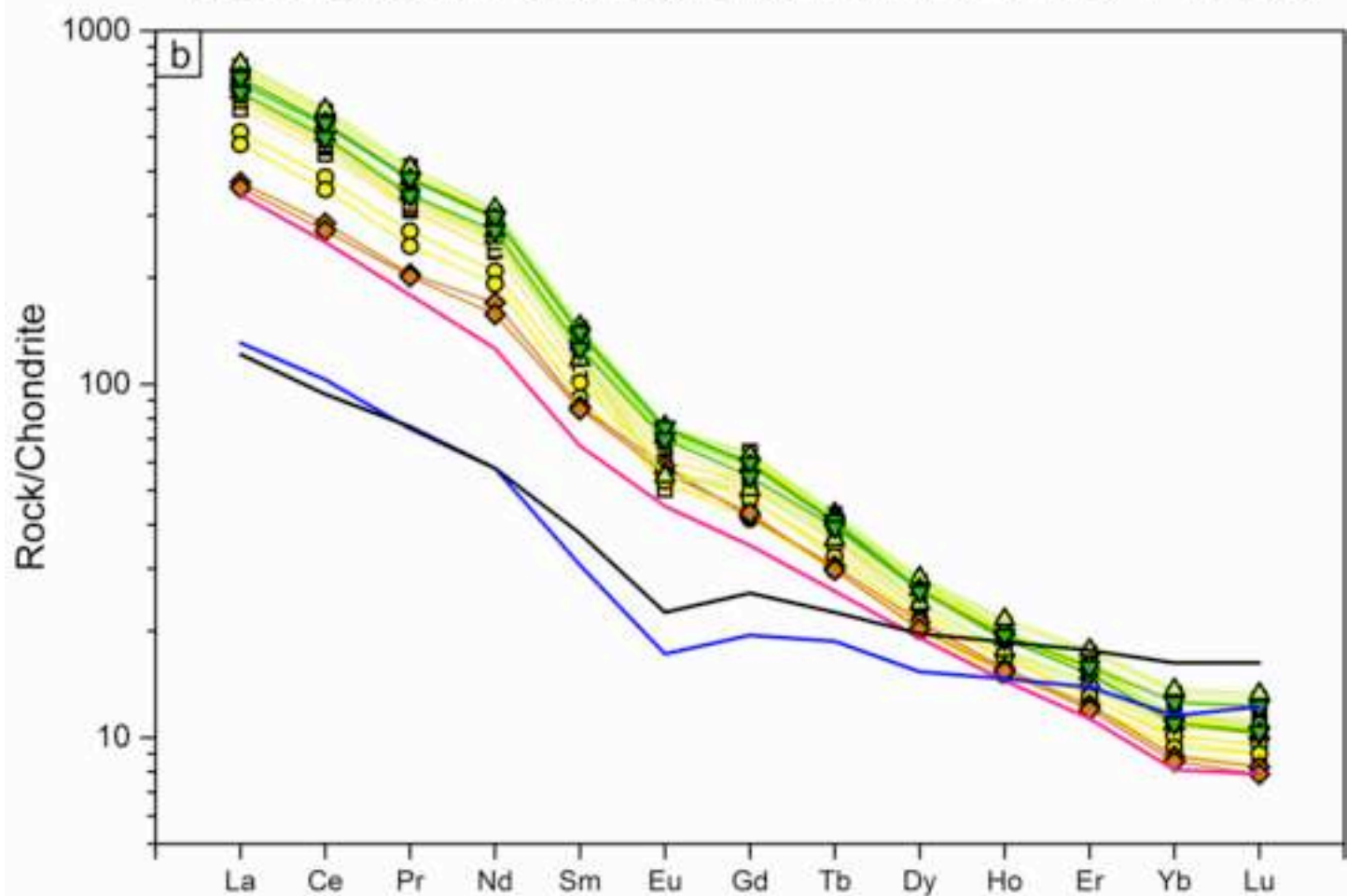
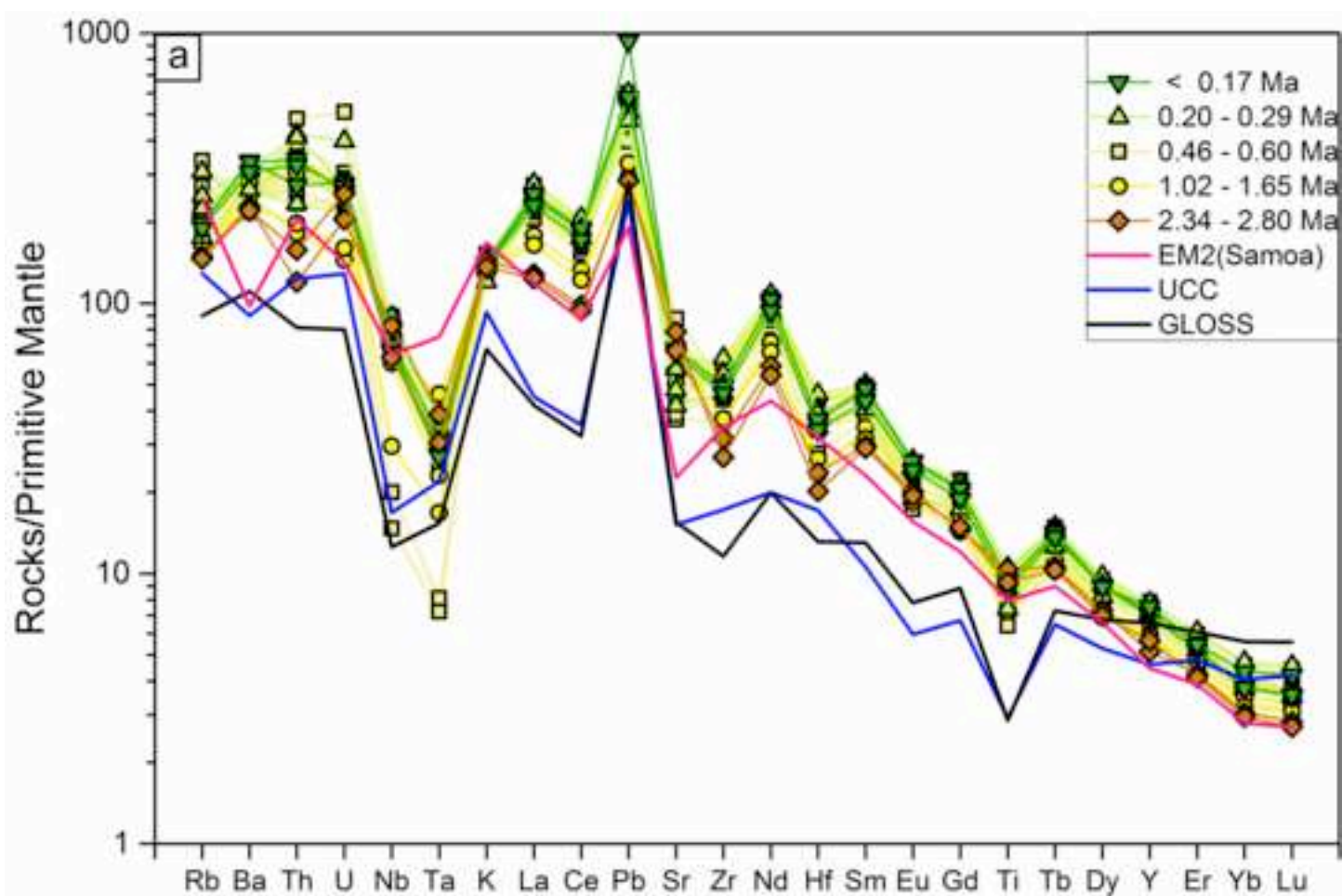


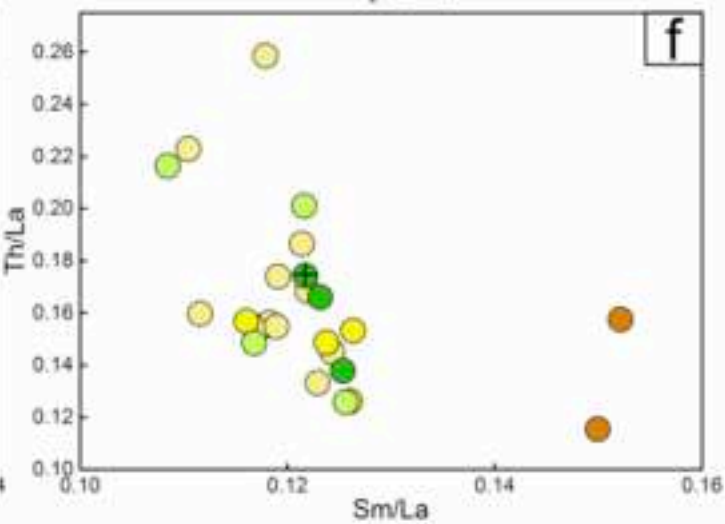
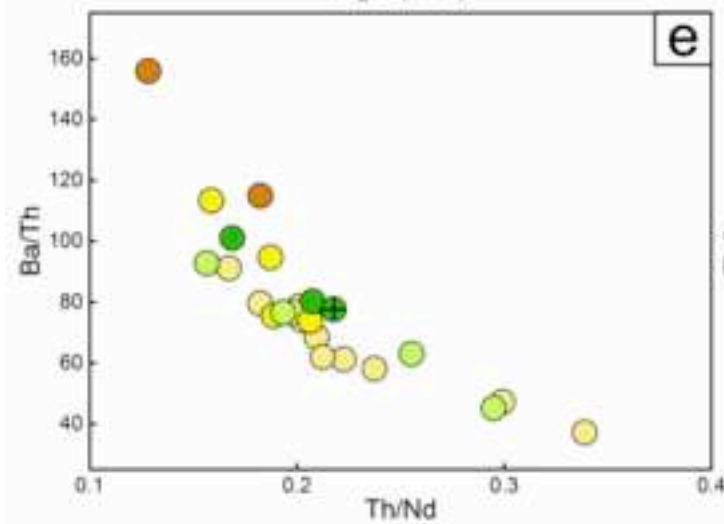
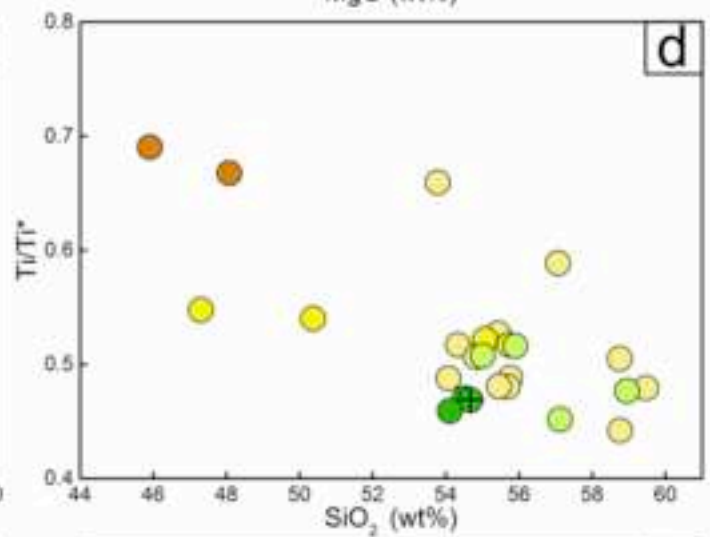
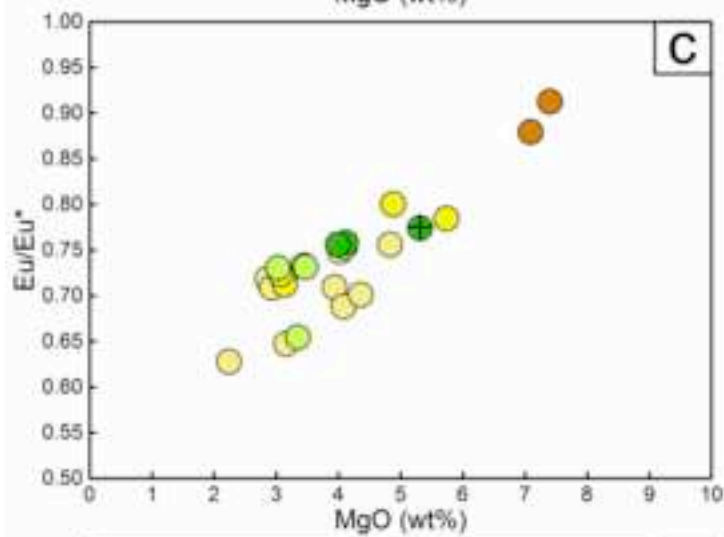
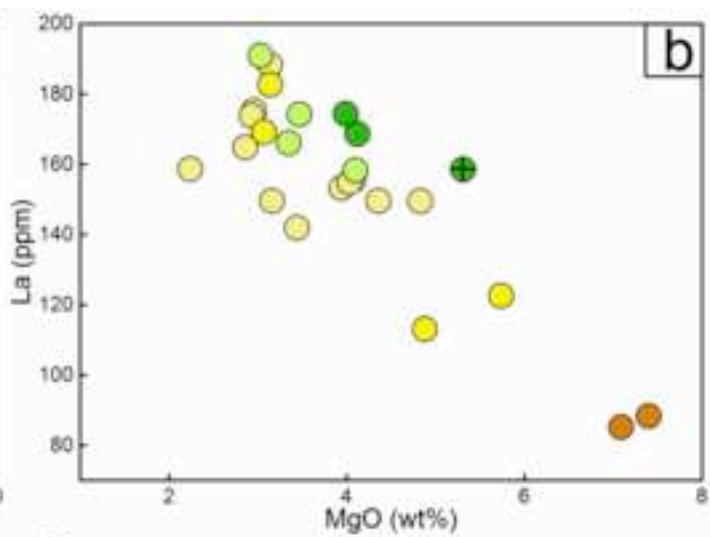
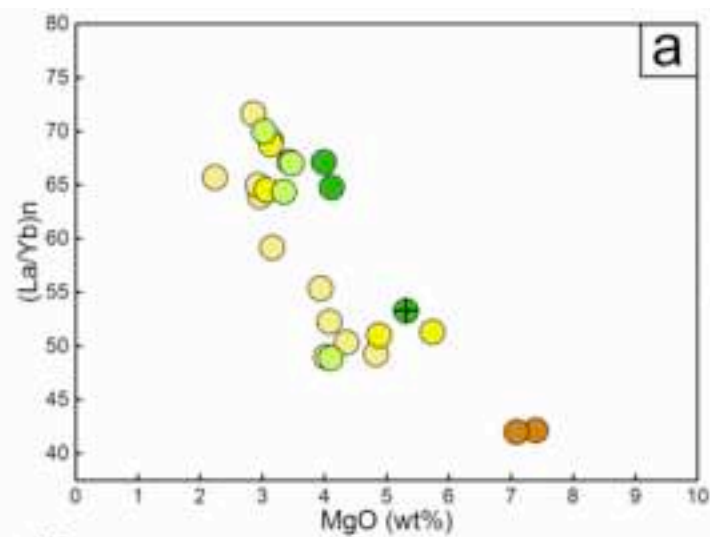


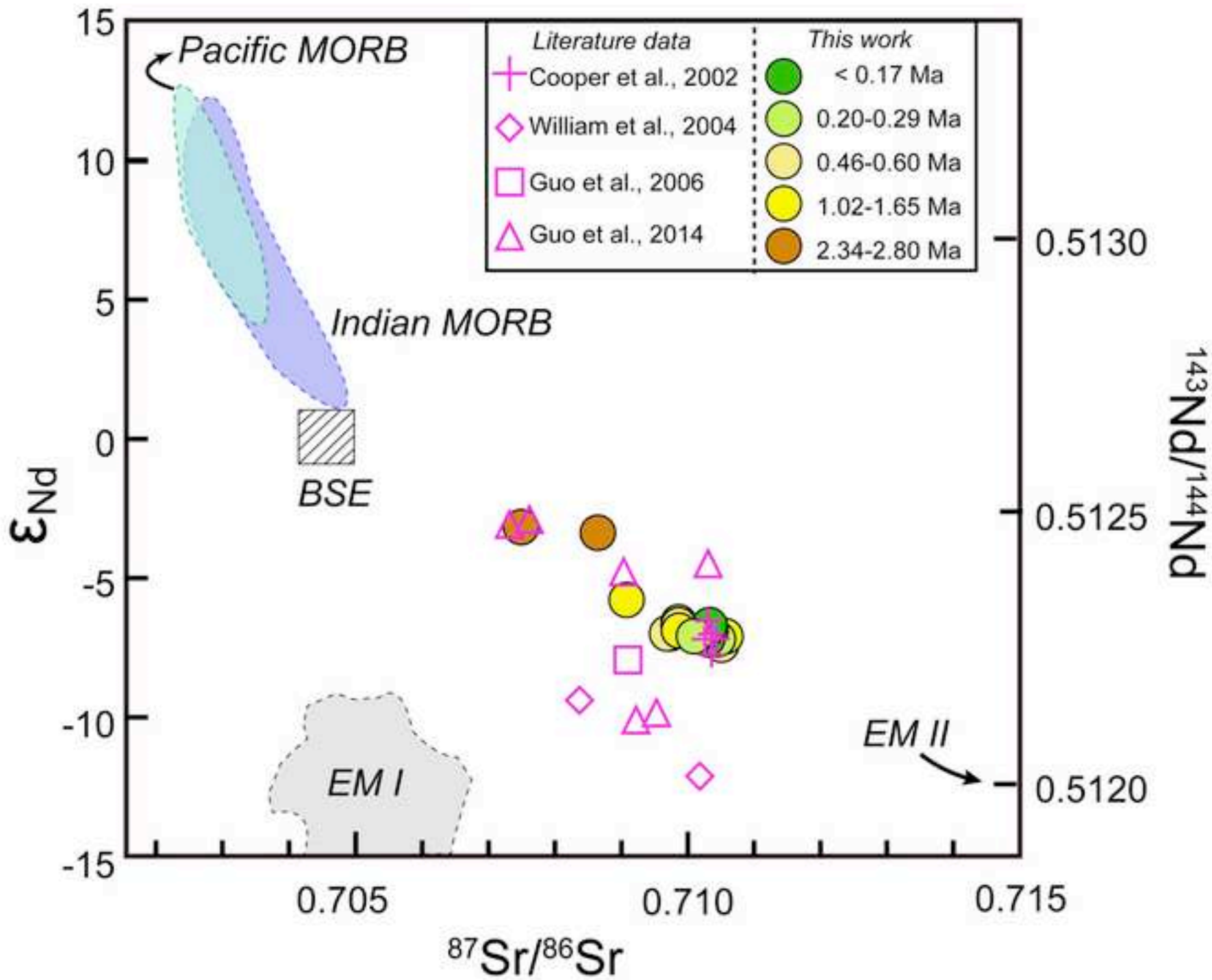


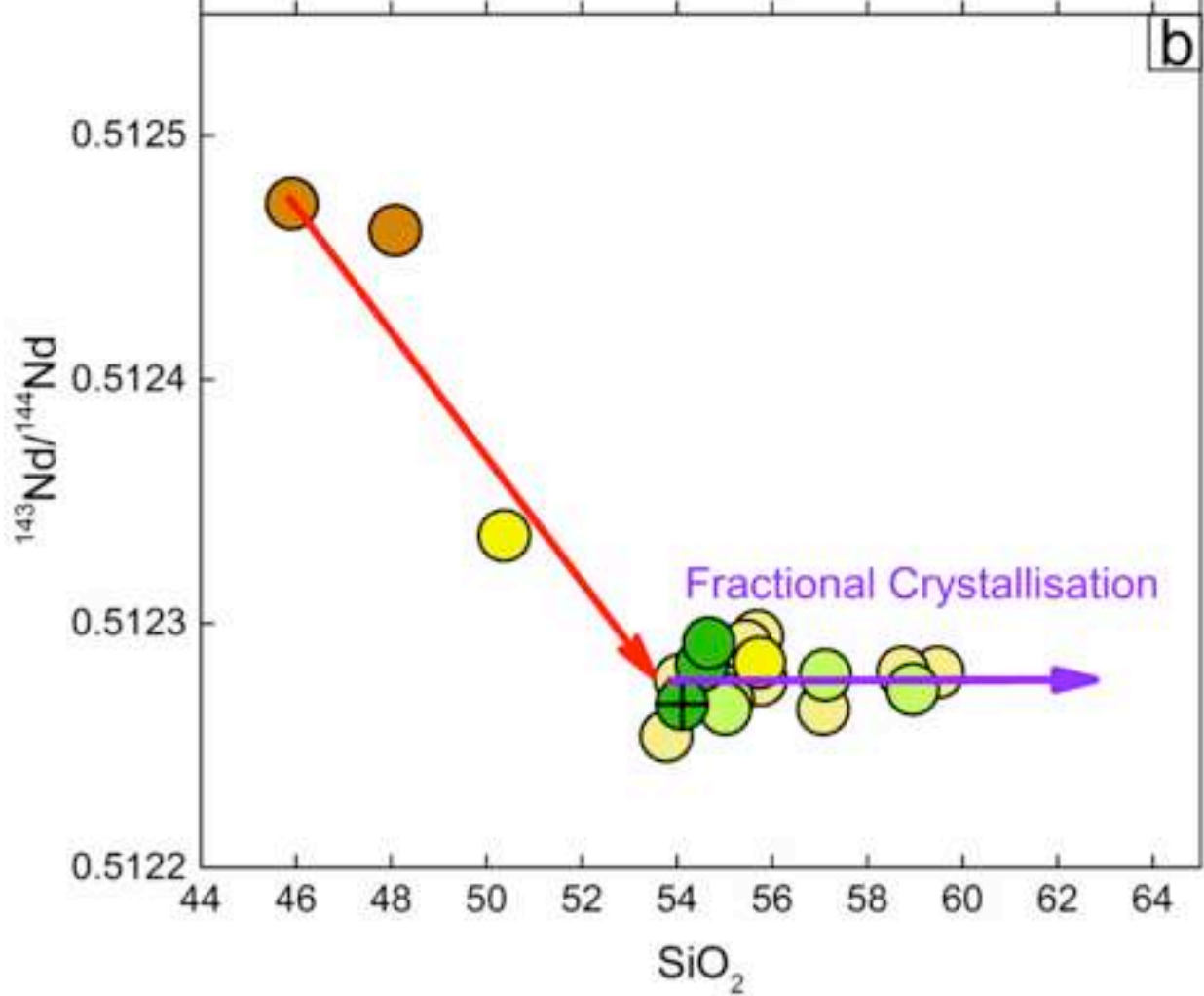
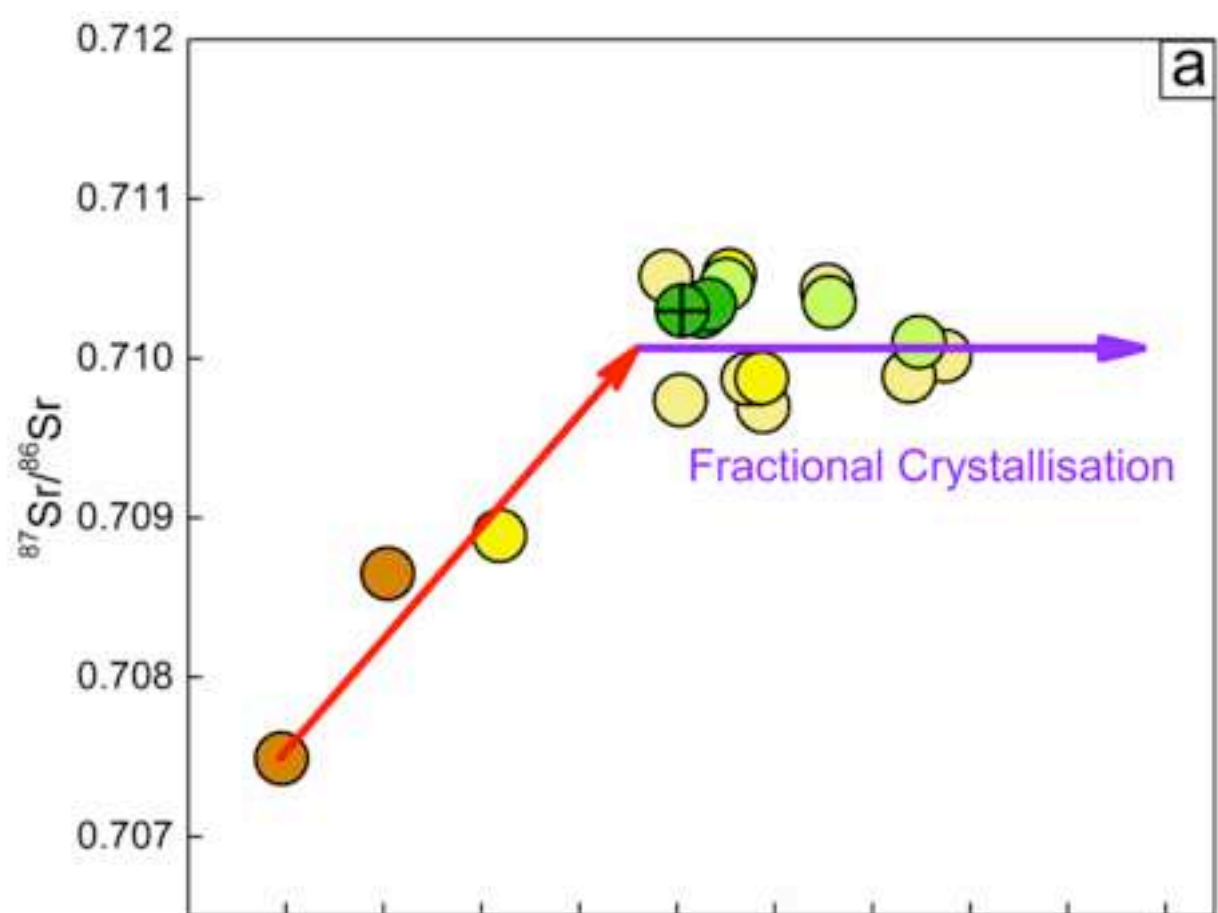


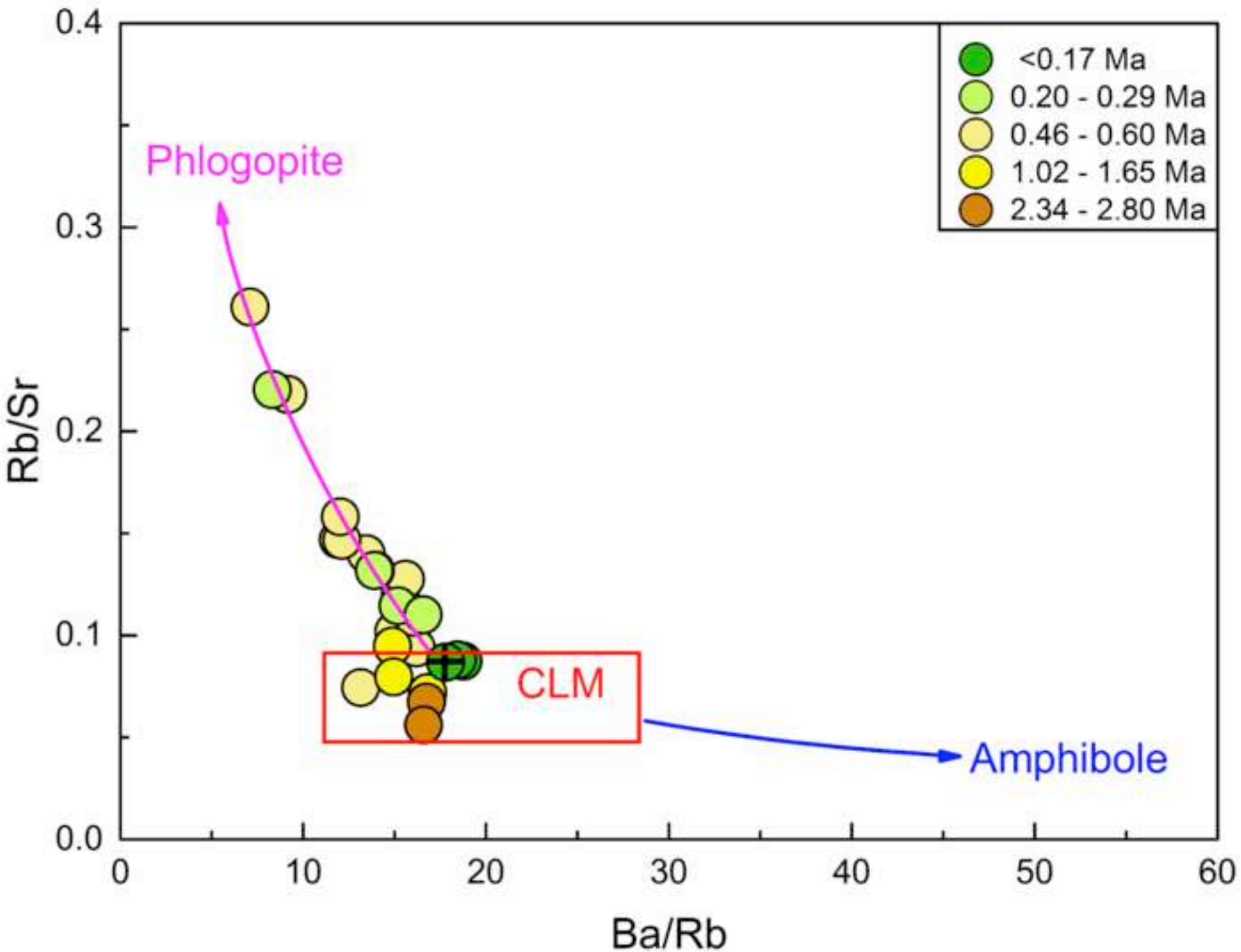












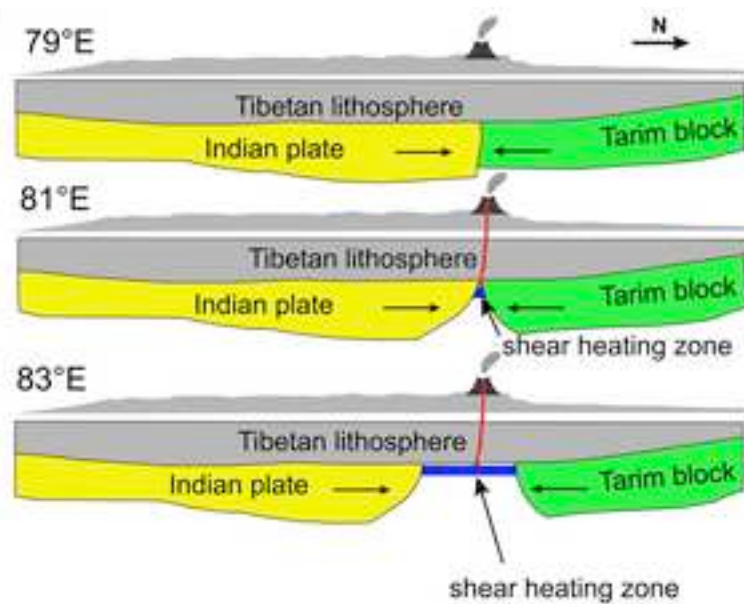
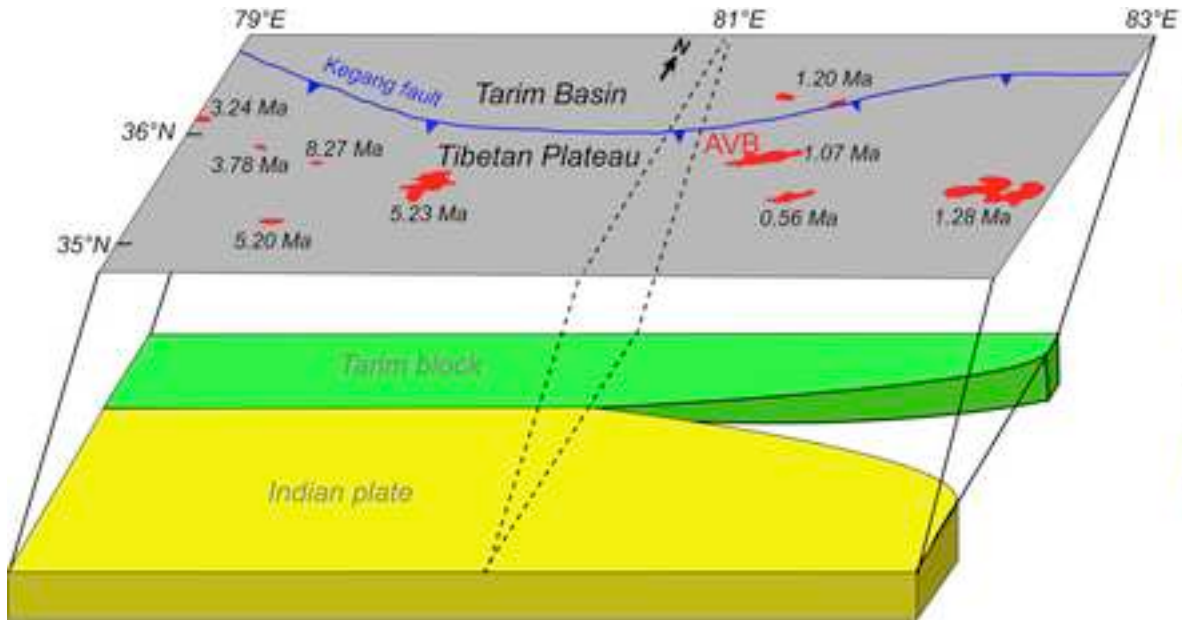


**Table 1**

Percentage abundance of vesicles, groundmass and phenocrysts in Ashikule volcanic rocks.

Episode (age)	Sample	Vesicle	Groundmass	Phenocrysts	Groundmass
1 and 2 (<0.17 Ma)	ASKL-3	60%	28%	Pl(6)+Cpx(3)+Opx(2)+Ol(1)	G
1 and 2 (<0.17 Ma)	ASKL-4	55%	32%	Pl(1)+Cpx(4)+Opx(6)+Ol(1)+Bi(<1)+Fe-Ti(<1)	Pl+Ol+G
1 and 2 (<0.17 Ma)	518-5	35%	51%	Opx(9)+Cpx(4)+Pl(1)	Pl+Cpx+Opx+G
3 (0.20-0.29 Ma)	ASKL-10	30%	60%	Pl(8)+Opx(1)+Fe-Ti(1)	Pl+Opx+Fe-Ti+G
3 (0.20-0.29 Ma)	513-11	45%	40%	Pl(10)+Cpx(2)+Opx(2)+Phl(1)	Pl+Cpx+Opx+G
3 (0.20-0.29 Ma)	516-19	20%	74%	Pl(4)+Opx(1)+Cpx(1)	Pl+Ol+Cpx+Opx+G
3 (0.20-0.29 Ma)	518-9	45%	39%	Pl(10)+Cpx(3)+Opx(2)+ Fe-Ti(1)	Pl+Cpx+Opx+Fe-Ti+G
4 (0.46-0.60 Ma)	ASKL-6	80%	15%	Pl(<1)+Cpx(3) +Opx(<1)+Ol(<1)+Fe-Ti(<1)	Fe-Ti+G
4 (0.46-0.60 Ma)	ASKL-7	20%	65%	Pl(12)+ Opx(2)+Cpx(<1)	G
4 (0.46-0.60 Ma)	ASKL-8	25%	42%	Pl(25)+ Opx(4)+Cpx(2)+ Fe-Ti(2)	Pl+Opx+Fe-Ti+G
4 (0.46-0.60 Ma)	ASKL-9	40%	38%	Pl(16) + Opx(5)+Cpx(1)+ Fe-Ti(<1)	Pl+Opx+Ol+Fe-Ti+G
4 (0.46-0.60 Ma)	ASKL-12	10%	58%	Pl(22)+ Opx(4)+Cpx(3)+Phl(1)+Fe-Ti(2)	Pl+OPX+CPX+Ol+G
4 (0.46-0.60 Ma)	ASKL-14	25%	66%	Pl(5)+Opx(4)	Pl+Opx+G
4 (0.46-0.60 Ma)	ASKL-15	30%	52%	Pl(7)+Cpx(6)+Opx(5)	Pl+Ol+Cpx+Opx+Fe-Ti+G
4 (0.46-0.60 Ma)	ASKL-16	15%	58%	Pl(15)+Opx(8)+Cpx(2)+Phl(1)+Fe-Ti(1)	Pl+Opx+Cpx+G
4 (0.46-0.60 Ma)	515-1	15%	68%	Pl(12 )+Opx(2)+Phl(2)+Cpx(1)	Pl+Phl+Cpx+Opx+G
4 (0.46-0.60 Ma)	WLK-3	30%	61%	Pl(6)+Opx(2)+Ol(<1)+Fe-Ti(<1)	Pl+Cpx+Opx+Fe-Ti+G
4 (0.46-0.60 Ma)	516-2	25%	56%	Cpx(11)+Opx(6)+Pl(2)	Pl+Cpx+Opx+G
4 (0.46-0.60 Ma)	516-22	40%	57%	Pl(2)+ Cpx(2)+Opx(1)	Pl+Cpx+G
5 (1.02-1.65 Ma)	ASKL-5	50%	34%	Pl(11)+ Opx(2)+Fe-Ti(2)+Cpx(1)	Pl+Cpx+G
5 (1.02-1.65 Ma)	516-11	40%	48%	Opx(6)+Cpx(3)+Pl(2)+Fe-Ti(1)	Pl+Cpx+Opx+G
5 (1.02-1.65 Ma)	516-12	50%	39%	Opx(6)+ Pl(4)+Cpx(1)	Pl+Cpx+G
5 (1.02-1.65 Ma)	518-14	30%	64%	Pl(2)+Opx(2)+Cpx(1)+Fe-Ti(1)	Pl+Cpx+Opx+Fe-Ti+G
6 (2.34-2.80 Ma)	ASKL-17	30%	57%	Cpx(9)+Opx(4)	Pl+Cpx+Opx+G
6 (2.34-2.80 Ma)	ASKL-18	30%	55%	Cpx(12)+Opx(2)+Pl(1)	Pl+Cpx+Opx+Fe-Ti+G

Pl = plagioclase; Cpx = clinopyroxene; Opx = orthopyroxene; Phl = phlogopite; Fe-Ti = Fe-Ti oxides; G = glass. Numbers in the brackets after the phenocrysts indicate the visually estimated volumetric percentages of the different phenocryst types in the thin section.

**Table 2**

Whole-rock trace and major element results for volcanic rocks from Ashikule Volcanoes.

Episode (age)	1 and 2 (<0.17 Ma)			3 (0.20-0.29 Ma)				4 (0.46-0.60 Ma)						
	Sample	ASKL-3	ASKL-4	518-5	ASKL-10	513-11	516-19	518-9	ASKL-6	ASKL-7	ASKL-8	ASKL-9	ASKL-12	ASKL-14
<i>(wt %)</i>														
SiO <sub>2</sub>	54.11	54.52	54.67	55.01	58.95	55.9	57.12	54.33	53.78	57.07	54.82	58.76	54.07	
TiO <sub>2</sub>	1.83	1.98	2.01	2.21	1.62	2.18	1.89	2.05	2.15	2.12	2.17	1.36	1.87	
Al <sub>2</sub> O <sub>3</sub>	14.57	14.43	14.49	14.59	14.97	14.77	14.65	14.78	14.44	14.89	14.67	14.19	14.16	
Fe <sub>2</sub> O <sub>3</sub> (T)	7.75	7.66	7.75	7.78	6.67	8.45	7.28	7.46	7.57	7.52	7.65	6.12	8.11	
MnO	0.11	0.11	0.11	0.11	0.09	0.12	0.1	0.10	0.11	0.10	0.11	0.09	0.12	
MgO	5.31	4.12	3.99	3.03	3.35	4.10	3.47	2.96	3.44	2.86	3.14	3.16	4.83	
CaO	5.46	6.56	6.62	6.39	5.24	6.50	5.63	5.88	6.26	5.71	6.16	5.97	7.20	
Na <sub>2</sub> O	3.18	3.08	3.12	3.25	3.4	3.11	3.14	3.05	3.19	3.27	3.24	2.88	2.92	
K <sub>2</sub> O	3.97	4.07	4.19	4.00	4.30	3.62	4.43	3.97	3.98	4.20	3.95	4.41	3.68	
P <sub>2</sub> O <sub>5</sub>	0.99	1.10	1.14	1.23	0.75	1.15	1.01	1.10	1.19	1.15	1.19	0.69	1.01	
LOI	2.91	1.48	0.96	1.45	1.27	0.60	1.01	3.70	2.86	1.03	2.68	2.99	1.20	
Total	100.19	99.11	99.05	99.05	100.61	100.5	99.93	99.38	98.97	99.92	99.78	100.6	99.2	
Mg#	61	55	54	47	53	52	52	47	51	46	48	54	57	
<i>(ppm)</i>														
Li	41.2	33.4	29.0	33.6	61.6	26.2	37.9	31.7	30.8	27.1	23.7	34.5	26.5	
Sc	14.5	6.31	9.74	10.9	11.0	8.97	11.2	11.0	8.06	8.92	10.7	10.7	9.42	
V	105	108	107	98.8	92.2	113	97.9	98.9	74.0	78.7	98.5	78.4	115	
Cr	78.5	66.1	66.2	24.6	49.2	71.5	52.9	26.3	14.8	19.0	22.9	75.3	104	
Co	20.0	19.7	19.3	16.6	17.5	20.6	17.5	16.4	12.0	12.5	16.9	13.5	22.9	
Ni	49.3	43.9	45.8	13.7	41.2	43.7	35.0	13.7	10.4	9.94	14.6	24.0	58.5	
Cu	19.8	20.8	20.0	18.8	26.4	25.3	20.9	10.2	17.7	13.7	16.9	14.3	26.5	
Zn	131	126	127	143	118	144	133	139	105	114	146	112	125	
Rb	120	125	126	143	195	111	159	136	112	134	143	171	112	
Sr	1386	1433	1432	1247	885	1012	1203	1130	874	956	1400	786	1193	
Y	34.4	31.8	32.6	35.2	32.1	35.5	32.9	33.2	26.6	29.6	33.8	30.8	33.2	
Zr	520	555	549	703	521	613	561	562	530	602	610	411	521	
Nb	47.0	51.3	50.0	63.4	53.5	57.8	51.9	10.5	47.1	52.9	14.3	46.2	49.0	
Cs	3.22	3.27	2.92	2.55	9.42	1.90	4.24	3.80	2.25	2.76	2.69	5.07	2.35	
Ba	2144	2348	2322	2169	1620	1846	2205	2074	1740	1800	2136	1570	1814	
La	159	169	174	191	166	158	174	175	142	165	188	150	150	
Ce	305	329	336	367	311	310	335	334	273	315	362	285	289	
Pr	32.5	35.9	36.4	39.0	32.8	33.0	36.0	36.5	29.4	33.2	39.2	29.8	30.7	
Nd	127	138	140	147	122	127	137	132	110	126	143	111	119	
Sm	19.3	21.1	21.5	22.3	18.0	19.9	21.2	20.7	16.8	18.4	22.0	16.5	18.4	
Eu	4.05	4.33	4.38	4.41	3.18	4.11	4.18	4.08	3.33	3.57	4.35	2.91	3.80	
Gd	11.3	12.2	12.3	12.9	10.4	12.0	12.1	12.4	9.7	10.6	13.3	9.7	11.0	
Tb	1.47	1.51	1.54	1.61	1.36	1.57	1.54	1.50	1.24	1.33	1.60	1.27	1.46	
Dy	6.58	6.60	6.69	7.10	6.07	7.21	6.66	6.67	5.38	5.87	6.91	5.81	6.64	
Ho	1.10	1.07	1.08	1.14	1.00	1.22	1.08	1.12	0.87	0.95	1.14	0.96	1.13	
Er	2.62	2.51	2.50	2.65	2.37	2.93	2.51	2.57	2.04	2.19	2.58	2.31	2.71	
Yb	2.14	1.87	1.86	1.96	1.85	2.32	1.87	1.97	1.52	1.65	1.96	1.81	2.18	
Lu	0.31	0.26	0.26	0.28	0.26	0.34	0.26	0.28	0.22	0.23	0.27	0.26	0.32	
Hf	10.5	11.5	11.5	14.3	10.7	12.6	12.1	10.8	10.7	11.8	12.0	8.64	10.8	
Ta	1.11	1.32	1.14	1.59	1.38	1.57	1.23	0.30	1.04	1.15	0.33	1.08	1.56	
Tl	8.26	0.66	0.73	0.81	0.15	0.64	0.95	0.29	0.15	1.96	0.62	1.29	0.83	
Pb	66.3	39.6	41.2	41.1	36.2	33.7	42.7	39.0	31.4	28.3	42.1	42.2	33.3	
Th	27.6	23.2	29.0	28.3	35.9	19.9	35.0	27.2	22.2	26.3	28.9	33.3	19.9	
U	5.67	5.87	5.47	5.59	8.39	4.51	5.76	4.88	4.67	5.11	5.65	6.41	5.14	

**Table 2 (continued)**

Episode (age)	4 (0.46-0.60 Ma)						5 (1.02-1.65 Ma)				6 (2.34-2.80 Ma)	
Sample	ASKL-15	ASKL-16	515-1	WLK-3	516-2	516-22	ASKL-5	516-11	516-12	518-14	ASKL-17	ASKL-18
<i>(wt %)</i>												
SiO <sub>2</sub>	55.76	55.69	59.48	58.75	55.45	55.43	55.07	50.37	47.3	55.73	48.08	45.91
TiO <sub>2</sub>	1.76	1.73	1.61	2.14	1.74	2.13	2.13	1.73	1.53	2.17	2.22	2.14
Al <sub>2</sub> O <sub>3</sub>	14.11	14.00	14.14	14.93	13.75	14.6	14.74	13.39	12.69	14.36	14.74	14.27
Fe <sub>2</sub> O <sub>3</sub> (T)	7.40	7.51	5.96	7.73	7.67	8.30	7.51	7.70	6.92	7.65	10.04	9.55
MnO	0.11	0.11	0.08	0.11	0.11	0.12	0.10	0.10	0.09	0.10	0.14	0.13
MgO	3.94	4.08	2.24	2.93	4.36	4.03	3.14	5.74	4.88	3.07	7.40	7.09
CaO	6.78	6.85	5.30	5.15	6.93	6.49	6.30	7.83	9.39	5.69	7.67	8.58
Na <sub>2</sub> O	2.95	2.89	3.23	3.31	2.83	3.04	3.30	2.91	2.95	3.21	3.87	3.65
K <sub>2</sub> O	3.94	3.74	4.47	4.34	3.76	3.65	4.03	3.72	3.48	4.13	4.30	3.95
P <sub>2</sub> O <sub>5</sub>	0.91	0.88	0.83	1.16	0.89	1.12	1.16	0.89	0.77	1.19	1.12	1.07
LOI	1.54	1.49	1.95	0.26	1.38	0.57	1.5	3.21	5.93	1.64	0.41	3.52
Total	99.20	98.97	99.29	100.81	98.87	99.48	98.98	97.59	95.93	98.94	99.99	99.86
Mg#	55	55	46	46	56	52	48	63	61	47	62	63
<i>(ppm)</i>												
Li	29.7	33.6	65.3	45.6	33.1	29.3	30.1	21.1	26.0	35.5	18.6	15.6
Sc	8.80	11.1	8.37	10.4	13.6	13.0	10.0	12.8	11.7	9.83	5.04	13.4
V	101	104	69.2	92.5	109	110	94.5	104	82.7	95.0	146	141
Cr	73.7	88.9	23.8	32.5	95.6	71.2	19.9	142	127	37.2	141	132
Co	20.6	19.2	11.8	16.3	20.2	20.1	15.3	26.5	23.7	16.2	36.9	35.6
Ni	57.7	38.4	11.5	22.8	51.5	46.4	10.4	122	118	21.2	122	107
Cu	23.8	19.3	15.5	22.1	23.6	25.9	15.4	24.5	41.8	18.1	32.7	31.0
Zn	121	125	128	146	125	167	137	112	95.9	146	111	109
Rb	138	139	214	151	134	112	142	104	106	140	95.0	92.8
Sr	1853	945	821	954	911	1025	1499	1451	1334	1062	1411	1657
Y	32.7	34.0	30.1	33.9	33.5	35.7	32.0	27.0	26.7	33.1	23.4	25.7
Zr	549	494	518	648	510	586	588	402	419	669	355	302
Nb	50.5	49.8	58.7	63.9	48.9	54.8	21.1	46.3	42.8	64.3	58.8	45.0
Cs	3.40	3.49	10.6	4.28	3.38	1.92	3.09	2.24	2.41	3.45	3.57	3.40
Ba	1813	1656	1519	1816	1619	1787	2115	1753	1590	1956	1590	1540
La	153	156	159	174	150	155	183	123	113	169	88.3	85.1
Ce	294	301	309	339	290	300	352	236	217	334	174	166
Pr	31.6	31.9	32.6	35.9	30.7	32.2	37.8	25.7	23.4	35.7	19.5	19.1
Nd	119	122	121	138	118	123	139	97.4	89.7	137	79.5	73.5
Sm	18.2	18.5	18.7	21.2	18.2	19.3	21.2	15.4	14.0	21.4	13.2	13.0
Eu	3.53	3.48	3.18	4.07	3.49	3.96	4.12	3.37	3.08	4.20	3.40	3.25
Gd	10.8	11.0	10.8	12.3	10.9	11.7	12.6	9.76	8.54	12.5	8.63	8.85
Tb	1.41	1.44	1.39	1.58	1.46	1.52	1.52	1.21	1.11	1.59	1.14	1.11
Dy	6.32	6.65	6.13	6.97	6.59	7.01	6.69	5.53	5.09	6.92	5.38	5.14
Ho	1.06	1.12	0.98	1.12	1.11	1.19	1.11	0.95	0.85	1.11	0.89	0.87
Er	2.57	2.66	2.30	2.56	2.66	2.87	2.50	2.16	2.03	2.55	2.05	1.99
Yb	1.99	2.14	1.73	1.92	2.13	2.27	1.91	1.71	1.59	1.88	1.50	1.45
Lu	0.29	0.31	0.24	0.27	0.31	0.33	0.27	0.24	0.23	0.26	0.21	0.20
Hf	11.0	10.5	11.1	13.3	10.5	12.2	11.6	7.21	8.26	13.7	7.31	6.24
Ta	1.13	1.13	1.55	1.49	1.12	1.21	0.69	1.89	0.95	1.54	1.59	1.25
Tl	0.76	0.76	1.25	0.62	0.78	0.60	0.73	0.42	0.64	0.96	0.29	0.28
Pb	35.9	35.8	42.7	37.0	34.2	32.3	40.7	20.9	23.5	41.2	20.1	20.3
Th	23.7	27.1	41.0	29.3	27.9	22.5	28.6	15.5	16.8	25.9	10.2	13.4
U	6.09	5.29	10.73	5.98	5.51	4.51	5.69	3.04	3.36	5.45	4.29	5.33

**Table 3**

Present day Sr and Nd isotopic compositions of volcanic rocks from Ashikule Volcanoes.

Episode (age)	Sample	$^{87}\text{Sr}/^{86}\text{Sr}$	Error ( $2\sigma$ )	$^{143}\text{Nd}/^{144}\text{Nd}$	Error ( $2\sigma$ )	Ave. $^{143}\text{Nd}/^{144}\text{Nd}$	Ave. $\epsilon\text{Nd}$																																																																																																																																																																																
1 and 2 (<0.17 Ma)	ASKL-3	0.710300	0.000005	0.512272	0.000011	0.512267	-7.1																																																																																																																																																																																
				0.512262	0.000010			1 and 2 (<0.17 Ma)	ASKL-4	0.710295	0.000005	0.512283	0.000010	0.512283	-6.8	0.512283	0.000012	1 and 2 (<0.17 Ma)	518-5	0.710337	0.000005	0.512290	0.000008	0.512292	-6.6	0.512293	0.000011	3 (0.20-0.29 Ma)	ASKL-10	0.710463	0.000005	0.512276	0.000012	0.512265	-7.1	0.512256	0.000010	0.512263	0.000016	3 (0.20-0.29 Ma)	513-11	0.710102	0.000005	0.512275	0.000010	0.512273	-7.0	0.512271	0.000009	3 (0.20-0.29 Ma)	518-9	0.710353	0.000005	0.512281	0.000010	0.512279	-6.8	0.512277	0.000011	4 (0.46-0.60 Ma)	ASKL-7	0.710516	0.000005	0.512259	0.000012	0.512254	-7.3	0.512250	0.000012	4 (0.46-0.60 Ma)	ASKL-8	0.710427	0.000005	0.512265	0.000011	0.512265	-7.1	0.512264	0.000010	4 (0.46-0.60 Ma)	ASKL-14	0.709738	0.000005	0.512277	0.000013	0.512277	-6.9	0.512278	0.000010	4 (0.46-0.60 Ma)	ASKL-15	0.709696	0.000005	0.512275	0.000009	0.512277	-6.9	0.512280	0.000011	4 (0.46-0.60 Ma)	ASKL-16	0.709871	0.000006	0.512295	0.000009	0.512295	-6.5	4 (0.46-0.60 Ma)	515-1	0.710016	0.000005	0.512280	0.000009	0.512280	-6.8	4 (0.46-0.60 Ma)	WLK-3	0.709887	0.000005	0.512288	0.000011	0.512280	-6.8	0.512273	0.000011	4 (0.46-0.60 Ma)	516-2	0.709870	0.000005	0.512291	0.000011	0.512291	-6.6	5 (1.02-1.65 Ma)	ASKL-5	0.710523	0.000005	0.512265	0.000010	0.512269	-7.0	0.512272	0.000014	5 (1.02-1.65 Ma)	516-11	0.708887	0.000005	0.512337	0.000012	0.512336	-5.7	0.512330	0.000010	0.512342	0.000014	5 (1.02-1.65 Ma)	518-14	0.709876	0.000005	0.512291	0.000010	0.512284	-6.8	0.512271	0.000009	0.512289	0.000014	6 (2.34-2.80 Ma)	ASKL-17	0.708650	0.000005	0.512449	0.000010	0.512461	-3.3	0.512473	0.000013	6 (2.34-2.80 Ma)	ASKL-18	0.707490	0.000005	0.512487	0.000010
1 and 2 (<0.17 Ma)	ASKL-4	0.710295	0.000005	0.512283	0.000010	0.512283	-6.8																																																																																																																																																																																
				0.512283	0.000012			1 and 2 (<0.17 Ma)	518-5	0.710337	0.000005	0.512290	0.000008	0.512292	-6.6	0.512293	0.000011	3 (0.20-0.29 Ma)	ASKL-10	0.710463	0.000005	0.512276	0.000012	0.512265	-7.1	0.512256	0.000010					0.512263	0.000016			3 (0.20-0.29 Ma)	513-11	0.710102	0.000005	0.512275	0.000010	0.512273	-7.0	0.512271	0.000009	3 (0.20-0.29 Ma)	518-9	0.710353	0.000005	0.512281	0.000010	0.512279	-6.8	0.512277	0.000011	4 (0.46-0.60 Ma)	ASKL-7	0.710516	0.000005	0.512259	0.000012	0.512254	-7.3	0.512250	0.000012	4 (0.46-0.60 Ma)	ASKL-8	0.710427	0.000005	0.512265	0.000011	0.512265	-7.1	0.512264	0.000010	4 (0.46-0.60 Ma)	ASKL-14	0.709738	0.000005	0.512277	0.000013	0.512277	-6.9	0.512278	0.000010	4 (0.46-0.60 Ma)	ASKL-15	0.709696	0.000005	0.512275	0.000009	0.512277	-6.9	0.512280	0.000011	4 (0.46-0.60 Ma)	ASKL-16	0.709871	0.000006	0.512295	0.000009	0.512295	-6.5	4 (0.46-0.60 Ma)	515-1	0.710016	0.000005	0.512280	0.000009	0.512280	-6.8	4 (0.46-0.60 Ma)	WLK-3	0.709887	0.000005	0.512288	0.000011	0.512280	-6.8	0.512273	0.000011	4 (0.46-0.60 Ma)	516-2	0.709870	0.000005	0.512291	0.000011	0.512291	-6.6	5 (1.02-1.65 Ma)	ASKL-5	0.710523	0.000005	0.512265	0.000010	0.512269	-7.0	0.512272	0.000014	5 (1.02-1.65 Ma)	516-11	0.708887	0.000005					0.512337	0.000012			0.512336	-5.7	0.512330	0.000010					0.512342	0.000014			5 (1.02-1.65 Ma)	518-14	0.709876	0.000005	0.512291	0.000010	0.512284	-6.8	0.512271	0.000009	0.512289	0.000014	6 (2.34-2.80 Ma)	ASKL-17					0.708650	0.000005
1 and 2 (<0.17 Ma)	518-5	0.710337	0.000005	0.512290	0.000008	0.512292	-6.6																																																																																																																																																																																
				0.512293	0.000011			3 (0.20-0.29 Ma)	ASKL-10	0.710463	0.000005	0.512276	0.000012	0.512265	-7.1	0.512256	0.000010					0.512263	0.000016			3 (0.20-0.29 Ma)	513-11	0.710102	0.000005	0.512275	0.000010	0.512273	-7.0	0.512271	0.000009	3 (0.20-0.29 Ma)	518-9	0.710353	0.000005	0.512281	0.000010	0.512279	-6.8	0.512277	0.000011	4 (0.46-0.60 Ma)	ASKL-7	0.710516	0.000005	0.512259	0.000012	0.512254	-7.3	0.512250	0.000012	4 (0.46-0.60 Ma)	ASKL-8	0.710427	0.000005	0.512265	0.000011	0.512265	-7.1	0.512264	0.000010	4 (0.46-0.60 Ma)	ASKL-14	0.709738	0.000005	0.512277	0.000013	0.512277	-6.9	0.512278	0.000010	4 (0.46-0.60 Ma)	ASKL-15	0.709696	0.000005	0.512275	0.000009	0.512277	-6.9	0.512280	0.000011	4 (0.46-0.60 Ma)	ASKL-16	0.709871	0.000006	0.512295	0.000009	0.512295	-6.5	4 (0.46-0.60 Ma)	515-1	0.710016	0.000005	0.512280	0.000009	0.512280	-6.8	4 (0.46-0.60 Ma)	WLK-3	0.709887	0.000005	0.512288	0.000011	0.512280	-6.8	0.512273	0.000011	4 (0.46-0.60 Ma)	516-2	0.709870	0.000005	0.512291	0.000011	0.512291	-6.6	5 (1.02-1.65 Ma)	ASKL-5	0.710523	0.000005	0.512265	0.000010	0.512269	-7.0	0.512272	0.000014	5 (1.02-1.65 Ma)	516-11	0.708887	0.000005	0.512337	0.000012	0.512336	-5.7	0.512330	0.000010					0.512342	0.000014	5 (1.02-1.65 Ma)	518-14	0.709876	0.000005	0.512291	0.000010			0.512284	-6.8	0.512271	0.000009	0.512289	0.000014	6 (2.34-2.80 Ma)	ASKL-17	0.708650	0.000005					0.512449	0.000010			0.512461	-3.3	0.512473	0.000013	6 (2.34-2.80 Ma)	ASKL-18	0.707490	0.000005	0.512487	0.000010	0.512472	-3.1
3 (0.20-0.29 Ma)	ASKL-10	0.710463	0.000005	0.512276	0.000012	0.512265	-7.1																																																																																																																																																																																
				0.512256	0.000010																																																																																																																																																																																		
				0.512263	0.000016																																																																																																																																																																																		
3 (0.20-0.29 Ma)	513-11	0.710102	0.000005	0.512275	0.000010	0.512273	-7.0																																																																																																																																																																																
				0.512271	0.000009																																																																																																																																																																																		
3 (0.20-0.29 Ma)	518-9	0.710353	0.000005	0.512281	0.000010	0.512279	-6.8																																																																																																																																																																																
				0.512277	0.000011																																																																																																																																																																																		
4 (0.46-0.60 Ma)	ASKL-7	0.710516	0.000005	0.512259	0.000012	0.512254	-7.3																																																																																																																																																																																
				0.512250	0.000012																																																																																																																																																																																		
4 (0.46-0.60 Ma)	ASKL-8	0.710427	0.000005	0.512265	0.000011	0.512265	-7.1																																																																																																																																																																																
				0.512264	0.000010																																																																																																																																																																																		
4 (0.46-0.60 Ma)	ASKL-14	0.709738	0.000005	0.512277	0.000013	0.512277	-6.9																																																																																																																																																																																
				0.512278	0.000010																																																																																																																																																																																		
4 (0.46-0.60 Ma)	ASKL-15	0.709696	0.000005	0.512275	0.000009	0.512277	-6.9																																																																																																																																																																																
				0.512280	0.000011																																																																																																																																																																																		
4 (0.46-0.60 Ma)	ASKL-16	0.709871	0.000006	0.512295	0.000009	0.512295	-6.5																																																																																																																																																																																
4 (0.46-0.60 Ma)	515-1	0.710016	0.000005	0.512280	0.000009	0.512280	-6.8																																																																																																																																																																																
4 (0.46-0.60 Ma)	WLK-3	0.709887	0.000005	0.512288	0.000011	0.512280	-6.8																																																																																																																																																																																
				0.512273	0.000011																																																																																																																																																																																		
4 (0.46-0.60 Ma)	516-2	0.709870	0.000005	0.512291	0.000011	0.512291	-6.6																																																																																																																																																																																
5 (1.02-1.65 Ma)	ASKL-5	0.710523	0.000005	0.512265	0.000010	0.512269	-7.0																																																																																																																																																																																
				0.512272	0.000014																																																																																																																																																																																		
5 (1.02-1.65 Ma)	516-11	0.708887	0.000005	0.512337	0.000012	0.512336	-5.7																																																																																																																																																																																
				0.512330	0.000010																																																																																																																																																																																		
				0.512342	0.000014																																																																																																																																																																																		
5 (1.02-1.65 Ma)	518-14	0.709876	0.000005	0.512291	0.000010	0.512284	-6.8																																																																																																																																																																																
				0.512271	0.000009																																																																																																																																																																																		
				0.512289	0.000014																																																																																																																																																																																		
6 (2.34-2.80 Ma)	ASKL-17	0.708650	0.000005	0.512449	0.000010	0.512461	-3.3																																																																																																																																																																																
				0.512473	0.000013																																																																																																																																																																																		
6 (2.34-2.80 Ma)	ASKL-18	0.707490	0.000005	0.512487	0.000010	0.512472	-3.1																																																																																																																																																																																
				0.512461	0.000011																																																																																																																																																																																		
				0.512469	0.000011																																																																																																																																																																																		

$^{143}\text{Nd}/^{144}\text{Nd}$  of chondritic uniform reservoir (CHUR) (0.512630; Bouvier et al., 2008) is used to calculate  $\epsilon\text{Nd}$ .